

# Mineral chemistry of magnetite from magnetite-apatite mineralization and their host rocks: examples from Kiruna, Sweden, and El Laco, Chile

Shannon G. Broughm<sup>1</sup> · John M. Hanchar<sup>1</sup> · Fernando Tornos<sup>2</sup> · Anne Westhues<sup>1</sup> · Samuel Attersley<sup>1</sup>

Received: 26 May 2016 / Accepted: 30 January 2017 / Published online: 13 March 2017  
© Springer-Verlag Berlin Heidelberg 2017

**Abstract** Interpretation of the mineralizing environment of magnetite-apatite deposits remains controversial with theories that include a hydrothermal or magmatic origin or a combination of those two processes. To address this controversy, we have analyzed the trace element content of magnetite from precisely known geographic locations and geologic environments from the Precambrian magnetite-apatite ore and host rocks in Kiruna, Sweden, and the Pliocene-Holocene El Laco volcano in the Atacama desert of Chile. Magnetite samples from Kiruna have low trace element concentrations with little chemical variation between the ore, host, and related intrusive rocks. Magnetite from andesite at El Laco, and dacite from the nearby Láscar volcano, has high trace element concentrations typical of magmatic magnetite. El Laco ore magnetite have low trace element concentrations and displays growth zoning in incompatible elements (Si, Ca, and Ce), compatible elements (Mg, Al, and Mn), large-ion lithophile element (Sr), and high field strength element (Y, Nb, and Th). The El Laco ore magnetite are similar in composition to magnetite that has been previously interpreted to have crystallized from hydrothermal fluids; however, there is a significant difference in the internal zoning patterns. At El Laco, each zoned

element is either enriched or depleted in the same layers, suggesting the magnetite crystallized from a volatile-rich, iron-oxide melt. In general, the compositions of magnetite from these two deposits plot in very wide fields that are not restricted to the proposed fields in published discriminant diagrams. This suggests that the use of these diagrams and genetic models based on them should be used with caution.

**Keywords** Magnetite · Magnetite-apatite deposits · Kiruna-type deposits · El Laco · Magmatic-hydrothermal

## Introduction

Genetic models for the formation of Kiruna-type magnetite-apatite deposits have been discussed and debated for over a century (e.g., Geijer 1910, 1919; Parák 1975; Frietsch 1978; Nyström and Henríquez 1994; Bergman et al. 2001). How these deposits relate to their adjacent host rocks and the relationship of the ore mineralization with hydrothermal alteration remains controversial (Hitzman et al. 1992; Williams et al. 2005; Groves et al. 2010). Additional research is necessary in order to obtain a better understanding of the processes involved in forming these deposits and how they relate, if at all, to other types of ore deposits (e.g., Fe-Ti oxide, iron oxide copper gold [IOCG], porphyry copper, skarn, volcanogenic massive sulfide [VMS]) (Williams et al. 2005; Dupuis and Beaudoin 2011; Nadoll et al. 2014). In the present study, the trace element chemistry of magnetite from perhaps the two most representative, and well-known, magnetite-apatite deposits, and their respective host rocks, was determined. The first is from Kiruna in the Norrbotten region of northern Sweden, and the second is from El Laco in the Atacama desert region of northern Chile. In the case of the Kiirunavaara deposit in Kiruna, magnetite from related felsic intrusive rocks

Editorial handling: B. Lehmann

**Electronic supplementary material** The online version of this article (doi:10.1007/s00126-017-0718-8) contains supplementary material, which is available to authorized users.

✉ John M. Hanchar  
jhanchar@mun.ca

<sup>1</sup> Department of Earth Sciences, Memorial University of Newfoundland, St. John's NL A1B 3X5, Canada

<sup>2</sup> Centro de Astrobiología (CSIC-INTA), Ctra. Ajalvir, Km 4.5, Torrejón de Ardoz, 28850 Madrid, Spain

were also analyzed. In Chile, magnetite was also analyzed from volcanic ejecta of dacitic composition from the nearby Lascar volcano (~50 km NE of El Laco). The aim is to determine whether the trace element chemistry of magnetite can be used to aid in settling the dispute on the processes involved in magnetite-apatite mineralization, e.g., hydrothermal, or magmatic, or a combination of these two processes. All of the samples used in this study are from precisely known geographic locations and geologic environments allowing a spatial analysis of the magnetite textures and associated minerals together with their trace element compositions.

Magnetite-apatite deposits can have high ore grades (up to 65% Fe) and large sizes (e.g., ~2500 Mt of iron has been mined in Kiruna with 644-Mt proven and probable reserves (Bergman et al. 2001; LKAB 2015) and ~730 Mt of iron ore at El Laco [Mario Rojo, Compañía Minera del Pacifico, 2015 personal communication]), making them attractive targets for mining. Magnetite-apatite deposits are the most important ore deposits in the Norrbotten region of northern Sweden (Bergman et al. 2001). The earliest studies on magnetite-apatite ores were focused on Kiruna (e.g., Geijer 1910, 1935; Parák 1975; Frietsch 1978), where the expression “Kiruna-type” deposit was adopted for this class of low-Ti magnetite, apatite-rich iron ore (e.g., Hildebrand 1986; Mücke and Younessi 1994). Some later studies focused on the magnetite-apatite ores at El Laco in the Atacama desert region of northern Chile, a much younger deposit, which is often considered a modern and shallow (i.e., Pliocene-Holocene) equivalent of the magnetite-apatite deposits found at Kiruna (e.g., Park 1961; Nyström and Henríquez 1994; Nyström et al. 2008).

Magnetite-apatite deposits are sometimes included as an end-member in the IOCG class of deposits (e.g., Hitzman et al. 1992; Barton and Johnson 1996; Hitzman 2000; Sillitoe 2003). Both magnetite-apatite and IOCG deposits contain large volumes of distinctly low-Ti iron oxides within rocks that have undergone extensive alkali-calcic metasomatism by hydrothermal fluids. Magnetite-apatite deposits do not contain economic concentrations of Cu or Au and almost exclusively contain massive magnetite or both magnetite and hematite, while IOCG deposits may also contain iron-rich silicate phases (Parák 1975; Williams et al. 2005; Groves et al. 2010). In some locations, magnetite-apatite deposits and IOCG deposits occur spatially, but usually not temporally, associated with each other, although whether there is a genetic relationship between the formation of magnetite-apatite and IOCG deposits remains unresolved (e.g., Groves et al. 2010).

There are two genetic models, and a third that is a combination of the first two, for the formation of magnetite-apatite deposits today: (1) crystallization from iron-rich melts that were immiscible from a parental silicate melt and were emplaced at different depths or erupted and crystallized at the surface (e.g., Henríquez and Martin 1978; Nyström and

Henríquez 1994; Naslund et al. 2002; Alva-Valdivia et al. 2003; Nyström et al. 2008; Martinsson 2016), crystallization was accompanied by the exsolution of large amounts of magmatic-hydrothermal fluids (Tornos et al. 2016); (2) replacement of the host rocks by iron-rich hydrothermal fluids (e.g., Hitzman et al. 1992; Rhodes and Oreskes 1999; Hitzman 2000; Sillitoe and Burrows 2002; Edfelt et al. 2005; Groves et al. 2010; Valley et al. 2011; Dare et al. 2015); and (3) a magmatic-hydrothermal genesis with an early generation of phenocrysts of magnetite that separated and floated from a crystallizing andesite melt and later were overgrown by hydrothermal magnetite (e.g., Knipping et al. 2015). A sedimentary-exhalative origin was suggested by Parák (1975) but was not widely accepted (Frietsch 1978; Nyström et al. 2008) and will not be discussed further.

Field observations and geochemical data for magnetite-apatite deposits are arguably compatible with both magmatic and hydrothermal origins (Hitzman et al. 1992; Nyström and Henríquez 1994; Naslund et al. 2002). Field evidence at the El Laco ore bodies that strongly supports an ultimate magmatic origin for the mineralization, i.e., direct crystallization from an iron-rich melt, includes distinct magnetite volcanic flow structures, vesicles in the magnetite ore veins with chilled margins that crosscut the host andesite, and the presence of degassing tubes similar to textures observed in basaltic flows (Henríquez and Martin 1978; Nyström and Henríquez 1994; Naslund et al. 2002; Henríquez et al. 2003; Tornos et al. 2016).

Arguments that support a hydrothermal (metasomatic) origin at El Laco include the presence of, sometimes jigsaw-like, breccias in which the magnetite supports fragments of altered host andesite blocks, a feature that is explained by open-space filling of ascending hydrothermal fluids (Sillitoe and Burrows 2002). Brecciated contacts between the ore and hydrothermally altered host rocks are fairly common at other magnetite-apatite deposits (e.g., Kiruna, the Adirondacks/New York State, and Bafq/Iran; Geijer 1910; Bergman et al. 2001; Valley et al. 2011; Sabet-Mobarhan-Talab et al. 2015; Westhues et al. 2016). Metasomatism of the host rocks surrounding these deposits is strong evidence that hydrothermal fluids were present. In Kiruna, the host rocks are pervasively hydrothermally altered (Geijer 1910; Frietsch et al. 1997; Westhues et al. 2016); however, at El Laco, there is not always direct contact between the altered host rock and ore, suggesting that the hydrothermal alteration here may not be directly related to ore emplacement (Tornos et al. 2016).

The magmatic model for magnetite-apatite ores involves the existence of immiscible iron-rich melts that crystallized to produce the large volumes of massive magnetite. This type of melt is considered to be similar to nelsonite deposits, which have a 2:1 oxide:apatite ratio and contain abundant Ti in the form of mostly rutile ± ilmenite ± titanomagnetite (Philpotts 1967; Frietsch 1978; Kolker 1982; Dymek and Owens 2001). Kamenetsky et al. (2013) tracked the existence of a large

immiscibility gap between silica-rich felsic melts and silica-poor mafic melts. The mechanism through which the iron-rich melts efficiently segregate into the ore and a presumed residual parent silicate-rich melt at the scale of massive deposits like those in Kiruna or El Laco has not yet been determined or observed in the field (i.e., the magnetite-apatite ore and residual silicate-melt in contact with each other). However, immiscible iron-rich and silicate melts have been observed within melt inclusions in the host andesite rocks at El Laco (Tornos et al. 2016; Velasco et al. 2016).

Hydrothermal models for magnetite-apatite deposits are extrapolated from hydrothermal models for IOCG deposits, with the assumption that these two types of deposits are genetically similar (Barton and Johnson 2004). Two main fluid sources have been proposed: (1) hydrothermal fluids exsolved from a magmatic source (e.g., Sillitoe and Burrows 2002; Groves et al. 2010) or (2) derived from an external source (e.g., basinal brines) where igneous intrusions are a heat source for circulating fluids in the crust (e.g., Barton and Johnson 1996; Rhodes and Oreskes 1999). Each system would require the generation of saline, sulfur-poor, and oxidized fluids (Barton and Johnson 2004). It is possible that there are multiple sources for the fluids, and they may vary between different localities (Williams et al. 2005; Valley et al. 2011).

Magnetite is an abundant and widespread oxide mineral and occurs in igneous, sedimentary, hydrothermal, and metamorphic rock assemblages and different types of ore deposits (Lindsley 1991). Magnetite is a member of the spinel group of minerals, which have a cubic close-packing structure with tetrahedral ( $\text{Fe}^{2+}$ ) and octahedral ( $\text{Fe}^{3+}$ ) sites in coordination with oxygen anions and the general stoichiometry  $\text{Fe}^{2+}\text{Fe}^{3+}_2\text{O}_4$  (Buddington and Lindsley 1964; Lindsley 1976). A variety of lithophile and siderophile elements with similar ionic radii to  $\text{Fe}^{2+}$  and  $\text{Fe}^{3+}$  substitute in the magnetite structure (e.g., Mg, Al, Si, P, Ca, Ti, V, Cr, Mn, Co, Ni), though in certain favorable physicochemical conditions, chalcophile and other elements can also be incorporated (e.g., Cu, Zn, Ga, Sn, Ce) (Nadoll et al. 2014). Of special interest is the behavior of Ti; the solubility of Ti in magnetite is controlled by the redox state and temperature of the system (Lindsley 1976). Magnetite is known to be resistant to surface weathering, making it an ideal provenance indicator for mineral exploration and perhaps useful for genetic studies of ore deposits (Grigsby 1990; Dupuis and Beaudoin 2011; Dare et al. 2012; Nadoll et al. 2014).

Several previous studies have discussed magnetite trace-element chemistry from Kiruna, El Laco, and other magnetite-apatite deposits (e.g., Loberg and Horndahl 1983; Frietsch and Jan-Anders 1995; Muller et al. 2003; Dupuis and Beaudoin 2011; Dare et al. 2015); however, most of the magnetite samples used in these studies were not from precisely known locations within the ore and surrounding host rocks.

Some of these studies have proposed empirical plots in which the magnetite of different types of mineralization have a characteristic trace element signature. In these diagrams, magnetite from magnetite-apatite deposits have distinct trace element chemical compositions compared to magnetite from other deposit types, such as banded iron formations (BIFs), IOCG, nelsonite, porphyry Cu, and Fe-Ti-V deposits (e.g., Loberg and Horndahl 1983; Dupuis and Beaudoin 2011; Dare et al. 2014). Dare et al. (2015) proposed that the composition of the magnetite from the El Laco ore, which is different to that of the accessory magnetite in the unaltered host andesite, is consistent with a hydrothermal origin for the magnetite-apatite ore (e.g., Dare et al. 2015).

The present study uses newly obtained data on the magnetite trace element geochemistry to assess the practical use and limitations of the proposed empirical magnetite discrimination diagrams and whether they can be utilized in interpreting the mineralization style and ore genesis of magnetite-apatite deposits.

## Geologic background

### Kiruna geology and magnetite-apatite ores

There are over 40 known magnetite-apatite deposits located in the Norrbotten region, with Kiirunavaara being the largest estimated at nearly 2 Gt before extraction of high-grade iron ore averaging 30–70% Fe (e.g., Cliff et al. 1990; Hallberg et al. 2012; Martinsson et al. 2016; Westhues et al. 2016). The Kiirunavaara magnetite-apatite deposit is a tabular-shaped ore body approximately 5 km long, 100 m thick, and at least 1500 m deep that lies concordant within steeply dipping volcanic host rocks (e.g., Parák 1975; Blake 1992; Bergman et al. 2001; Harlov et al. 2002; Nyström et al. 2008).

The oldest unit in the Kiruna area are the Karelian (2.4–1.96 Ga) mafic-intermediate metavolcanic flows (Kiruna Greenstone Group), overlain by metasedimentary and intermediate-felsic metavolcanic rocks of the Svecofennian porphyry group (1.96–1.75 Ga) (Fig. 1a) (e.g., Bergman et al. 2001). The magnetite-apatite deposits in the Kiruna area are hosted by the metavolcanic rocks of the porphyry group (Parák 1975; Martinsson 2004). The Kiirunavaara-Luossavaara ore bodies follow the contact between thick trachyandesitic lava flows (footwall) and pyroclastic rhyodacites (hanging wall). The entire Norrbotten region has been subjected to greenschist facies metamorphism (Bergman et al. 2001) and is overprinted by regional-scale Na and Cl metasomatism in the form of albite and Cl-rich scapolite ( $\text{Na}_4\text{Al}_3\text{Si}_9\text{O}_{24}\text{Cl}-\text{Ca}_4\text{Al}_6\text{Si}_6\text{O}_{24}\text{CO}_3$ ) (Frietsch et al. 1997).

There is a syenite intrusion approximately 1 km stratigraphically below the Kiirunavaara ore body (Blake 1992; Bergman et al. 2001). Granophyric to granitic dikes

intrude the Kiirunavaara ore, and a larger body of potassic granite can be found within the footwall of the Kiirunavaara mine. New constraints on the ages of these intrusions show that the syenite ( $1880 \pm 7$  and  $1881 \pm 4$  Ma) is of a similar age to the metavolcanic host rocks ( $1884 \pm 4$  and  $1880 \pm 3$  Ma) and older than the ore ( $1877 \pm 4$  and  $1874 \pm 7$  Ma), while zircon from the granite ( $1874 \pm 7$  Ma) and two ore samples have overlapping ages (Westhues et al. 2016).

Two types of ore can be identified at Kiirunavaara based on their phosphorous content, primarily residing in apatite, the B ore ( $<0.05\%$  P) and D ore ( $>1\%$  P) (e.g., Bergman et al. 2001). The ore is rich in rare earth elements (REE), dominantly as light rare earth elements contained within the apatite or in inclusions of monazite in apatite, which is currently not mined (Hallberg et al. 2012). The contact with the host rocks is bounded by a magnetite-actinolite-filled breccia with veins that can be found extending tens of meters into the hanging wall (Bergman et al. 2001). The footwall at Kiirunavaara is strongly albitized, especially near the syenite intrusion, and here, widespread amygdales are found to contain secondary magnetite, actinolite, and titanite (Geijer 1910; Romer et al. 1994; Bergman et al. 2001).

The Tuollavaara and Per Geijer (e.g., Nukutusvaara and Rektorn) ore bodies are smaller than Kiirunavaara and are hosted within rhyodacites in the upper parts of the porphyry group (Martinsson 1994; Bergman et al. 2001). Hematite is more common in these smaller deposits than at Kiirunavaara. Similar to the Kiirunavaara deposit, contacts between the ore and host rocks are often brecciated (i.e., altered host rock fragments are surrounded by veins of iron oxides + apatite), and veining of iron ore commonly extends into both footwall and hanging wall up to tens of meters (Bergman et al. 2001).

### El Laco geology and magnetite-apatite ores

The El Laco andesite stratovolcano is located in the current active volcanic arc, the Central Volcanic Zone (CVZ), of the Andes in the Atacama desert of northern Chile (Fig. 1b). The volcano is made up of calc-alkaline andesite flows and pyroclastic rocks, with K-Ar dates from  $5.3 \pm 1.9$  to  $1.6 \pm 0.5$  Ma (Naranjo et al. 2010). There are seven high-grade iron ore bodies at El Laco that reach up to  $1 \text{ km}^2$  at the surface and exceeding 100-m thickness (Naslund et al. 2002). The dominant magnetite mineralization occurs as large stratabound lenses that are texturally massive, brecciated, vesicular or friable, and have been interpreted as lava flows or pyroclastic rocks. They are rooted in subvertical veins of massive and coarse-grained magnetite (Henríquez and Martín 1978; Nyström and Henríquez 1994; Naslund et al. 2002; Nyström et al. 2016; Tornos et al. 2016). The magnetite ore is associated with minor amounts of diopside, scapolite, and anhydrite (Tornos et al. 2016), while apatite is fairly uncommon in the stratabound ores but is abundant in the feeder dikes.

The magnetite-apatite ore bodies and some of the andesite host rocks have been pervasively overprinted by hydrothermal alteration that is thought to be broadly synchronous with the emplacement of the magnetite ore (see Fig. 1b). The andesite has been locally replaced by alkali-calcic hydrothermal assemblages, including diopside, K-feldspar, magnetite, anhydrite, and scapolite that are related to widespread brecciation of the altered andesite (Tornos et al. 2016). The andesite host and the alkali-calcic altered rocks are overprinted by a later and shallower steam-heated alteration that is observed as stratabound zones of dominantly alunite and gypsum (Sillitoe and Burrows 2002; Tornos et al. 2016). Late martitization related to the steam-heated alteration overprints large parts of the magnetite ore (Tornos et al. 2016).

### Láscar volcano

The Láscar volcano is located approximately 57 km northwest of El Laco ( $67^\circ 43' \text{ W}$ ,  $23^\circ 22' \text{ S}$ ) and is the most active volcano in the CVZ today with a significant eruption in 1993 and intermittent activity ever since (Tassi et al. 2009). Láscar is considered a typical arc-related volcano with andesitic to dacitic composition. The andesite-dacite at Láscar includes anhydrite phenocrysts as well as droplets of magnetite—no significant concentrations of massive magnetite have been described. The reason to compare the geochemistry of magnetite at El Laco and Láscar volcanoes is to determine if a difference exists with the magnetite from a volcano with massive magnetite mineralization, such as El Laco, with a similar volcano located within the same volcanic arc system that does not have visible massive magnetite deposits, such as Láscar.

### Analytical methods

#### Sample selection and preparation

The magnetite-bearing rocks of this study have been selected using a systematic sample collection that was carried out from magnetite-apatite ores and their respective host rocks in the Norrbotten region of northern Sweden and the El Laco and Láscar volcanoes (Fig. 1 and electronic supplementary material [ESM] Table 1A). The samples have been thoroughly examined using cross-polarized and reflected light microscopy on polished thin sections in order to select the samples with minimal replacement of magnetite by hematite. Magnetite grains were chosen in situ from the samples of ore, hanging wall, and footwall as well as from any spatially associated intrusive rocks. Some samples from the host rocks did not contain magnetite or the grains were not large enough for laser ablation analysis and therefore could not be included in this study (e.g., many of the more felsic hanging wall rocks at Kiruna and altered andesite at El Laco).

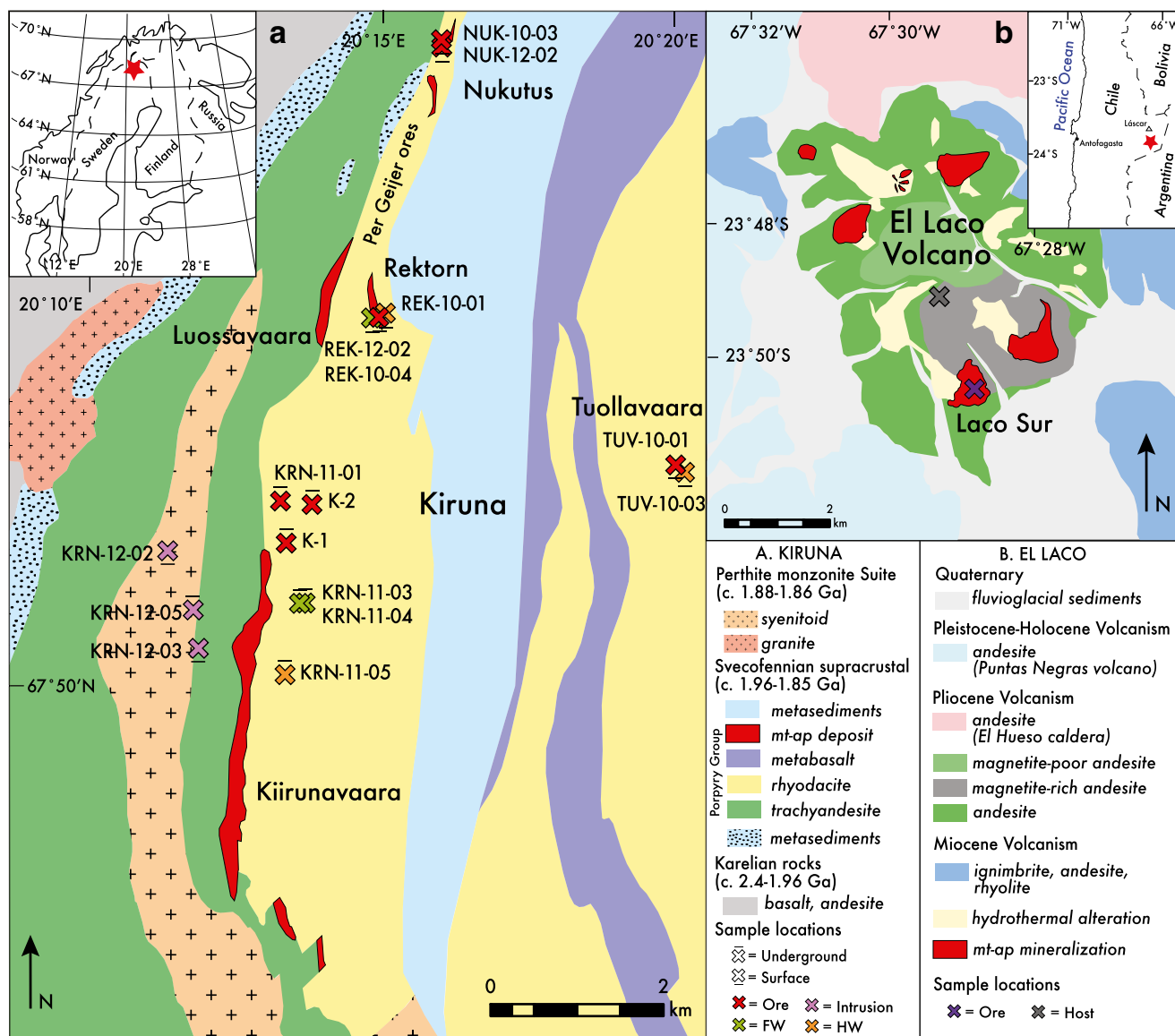


**Fig. 1** Simplified geological maps of the study areas. **a** Kiruna district, Norrbotten region, northern Sweden, with sample locations for this study. The Kiirunavaara magnetite-apatite deposit dips eastward between the footwall and hanging wall rock units. Samples collected underground within the mine are projected to the map surface and therefore appear to

the east of ore body (map modified after SGU data and Westhues et al. 2016). **b** El Laco volcano, ore samples from this study are from the Laco Sur deposit with one dacite sample from the Láscar volcano shown in the inset map (map modified after Tornos et al. 2016)

For Kiruna, samples that contain sufficient magnetite included all the ore samples from the Kiirunavaara high-P (KRN-10-02, K-1, and KRN-11-01) and low-P (K-2) ore and the selected smaller magnetite-apatite ores, Tuolluvaara (TUV-10-01), Nukutusvaara (NUK-12-02 and NUK-10-03), and Rektorn (REK-10-04). The Rektorn ore also contains abundant hematite, described further below. At Kiirunavaara, the footwall andesite rocks were magnetite rich, and there was an altered (KRN-11-04) and a less altered (KRN-11-03) sample chosen. One sample from the hanging wall rhyodacite rocks at Kiirunavaara contained a small amount of magnetite (KRN-11-05). Several samples containing magnetite from felsic intrusive

bodies spatially associated with the Kiirunavaara ore body were also chosen; these included an aplite vein (KRN-12-02), a syenite pluton (KRN-12-03), and a granite pluton from underground inside the mine (KRN-12-05). As mentioned above, the smaller magnetite-apatite bodies in the Kiruna area (i.e., Per Geijer ores Rektorn, Nukutus, and Tuolluvaara) are hosted in the rhyodacitic rocks that generally do not contain abundant magnetite. However, sufficiently sized magnetite was present in the host rock at Tuolluvaara (TUV-10-03). The Rektorn footwall (REK-12-02) contains abundant magnetite, and the Rektorn hanging wall was eliminated from this study because it contains abundant hematite.

At El Laco in the upper levels of the large magnetite-apatite ore body at Laco Sur, two massive magnetite ore samples were collected (ELL-14-04 and ELL-14-05). In the lower levels of the Laco Sur ore body (at approximately 4650-m elevation), a magnetite vein from a feeder structure was sampled (ELL-14-06). A sample of andesite from the El Laco volcano (ELL-14-02) and a dacite sample from Láscar (LAS-14-07) were also collected.

The magnetite-bearing samples selected ( $n = 17$  from Kiruna,  $n = 4$  from El Laco, and  $n = 1$  from Láscar) were first trimmed with a saw to remove any altered or weathered material and then mounted in 25-mm-diameter  $\times$  6-mm-tall epoxy pucks. These pucks were then polished and carbon coated and examined with a JEOL 7100F field emission scanning electron microscope (SEM) at Memorial University of Newfoundland equipped with energy-dispersive spectroscopy (EDS) at 15 kV and 50 nA. Magnetite grains, as well as any associated minerals, were identified using back-scattered electron (BSE) imaging; EDS; and conventional reflected light microscopy, which was the best way to distinguish between magnetite and hematite.

### Electron probe microanalyzer analyses

The iron content of the magnetite grains was measured using a JEOL JXA-8230 SuperProbe electron probe microanalyzer (EPMA) at Memorial University of Newfoundland. Details concerning the EPMA analyses are summarized in the ESM Table 2A. Quantitative chemical analyses of magnetite were done to obtain Fe concentrations in the same location as the laser ablation–inductively coupled plasma–mass spectrometry (LA-ICP-MS) analyses to use Fe as the internal standard for reducing the laser ablation data with Iolite software (Paton et al. 2011). The following conditions were used for the EPMA analyses: accelerating voltage of 15 kV, sample current of 100 nA, peak and background count times of 10 s, and a beam diameter of 3  $\mu\text{m}$ . Natural magnetite from the Astimex MINM25–53 mineral standards mount was used as a primary Fe standard. Raw X-ray intensities were corrected using standard ZAF techniques with the JEOL software.

### X-ray maps

X-ray maps of the Kiruna magnetite grains were made on one representative magnetite grain per sample for Al, Si, Ca, Ti, and V. Vanadium was mapped after variations in V were detected with EDS. Aluminum and Ti were also chosen because of their generally immobile nature in hydrothermal fluids. Silica and Ca were chosen for their highly mobile nature in hydrothermal fluids (Dare et al. 2014; Nadoll et al. 2014). For the El Laco samples, EPMA X-ray maps for Al, Si, Ca, V, and Mg were acquired on one representative magnetite grain per sample. For each map, an accelerating voltage of 15 kV, sample current of

250 nA, and a pixel dwell time of 150 ms were used. The map area, step size, and total time to create each map ranged from 150  $\mu\text{m}^2$  to 2  $\text{mm}^2$ , 0.4 to 1.0  $\mu\text{m}$ , and 4 to 10 h, respectively, depending on the size of the magnetite grain.

### LA-ICP-MS analyses

In situ LA-ICP-MS analyses were done at the MicroAnalysis Facility–Bruneau Innovation Centre (MAF-IIC) at Memorial University of Newfoundland using a Finnigan Element XR high-resolution, double-focusing magnetic sector–inductively coupled–plasma mass spectrometer (HR-ICP-MS), coupled to a GeoLas 193-nm Excimer laser system. Details for the LA-ICP-MS analyses are summarized in the ESM Table 2A. Zipkin et al. (2015) describes the current methodology in the LA-ICP-MS facility for trace element analysis using this equipment; these same methods were used in the present study with the modifications noted below.

A laser spot diameter of 30  $\mu\text{m}$  was used for all magnetite analyses, a 59- $\mu\text{m}$  spot was used for the primary calibration material NIST 610, and a 49- $\mu\text{m}$  spot for the secondary standard reference material BCR-2G. A total of 42 elements and 35 elements, respectively, were analyzed for each magnetite analysis during the Kiruna and El Laco LA-ICP-MS analyses. Magnetite samples from El Laco were analyzed prior to the Kiruna samples, and elements that were consistently below the limit of detection (LOD) were not measured during the Kiruna analyses after verifying that those elements were again not detectable. Instead, REEs were included for the Kiruna analyses in order to make a comparison with the well-constrained trace REE concentrations in the BCR-2G glass (Jochum et al. 2005). The laser energy density used for all laser ablation analyses was 3  $\text{J}/\text{cm}^2$  with a pulse frequency of 8 Hz. For each analysis, the background was measured for about 30 s, followed by 90 s of laser ablation, and washout was monitored for about 20 s after each ablation. Isotope signals  $^{57}\text{Fe}$ ,  $^{51}\text{V}$ , and  $^{9}\text{Co}$  were closely monitored during the day to track instrumental drift. For the El Laco ablation session, laser spots were taken across grains that showed zoning in BSE and X-ray maps. A total of 72 analyses were done on magnetite from El Laco and Láscar. Eighty-seven analyses were done on magnetite from the Kiruna area samples. A complete list of the analyses that were done is reported in the ESM.

The LA-ICP-MS data were reduced using the Iolite software (Paton et al. 2011) with the Fe concentration from the EPMA analysis used as the internal standard. Peaks for La, Ce, Al, Mg, Zr, Si, P, Ca, and Ti were monitored during the data reduction to avoid inclusions of other minerals (e.g., monazite, apatite, zircon, titanite) or inclusion of the host material in the case of tiny magnetite grains (e.g., feldspar, amphibole, quartz). The LOD for each of the elements measured was calculated in Iolite (Paton et al. 2011) using the method described in Zipkin et al. (2015). The LOD and mean results

of each isotope measured are listed in ESM Table 3A. The BCR-2G results from the Kiruna and El Laco analysis sessions show excellent correlation with the long-term running averages for BCR-2G collected over a span of 17 years at Memorial University (see ESM Fig. 1A and Secondary ICP-MS Standards 2).

## Results

### Kiruna magnetite textures and associated minerals

From the samples investigated at Kiirunavaara, the D ore (i.e., high-P ore) contains two types of magnetite: (1) massive magnetite with interstitial apatite, biotite, and later calcium carbonate (Fig. 2a) and (2) 20–200- $\mu\text{m}$  magnetite grains that are subhedral to anhedral with apatite as the dominant gangue mineral phase  $\pm$  actinolite, plagioclase, and quartz (Fig. 2b, c). The B ore (i.e., low-P ore; Fig. 2d) magnetite is massive with minor amounts of interstitial biotite, calcium carbonate, and apatite; thus, it contains less phosphorus than the D ore. The Kiirunavaara trachyandesitic footwall has large anhedral magnetite grains ranging in size from 100 to 300  $\mu\text{m}$  that are found in clusters as well as disseminated magnetite. The magnetite clusters are more abundant and larger (approximately 1 mm in diameter) in the altered footwall (Fig. 2e) compared to the less altered footwall (approximately 500  $\mu\text{m}$  in diameter). The hanging wall rocks at Kiirunavaara have a low abundance of magnetite with grains that are euhedral-subhedral and  $<60$   $\mu\text{m}$  (Fig. 2f). The aplite vein sample (KRN-12-02) has a low abundance of magnetite with grains that are  $<100$   $\mu\text{m}$ , fractured and associated with biotite, titanite, and zircon (Fig. 2g). The syenite sample (KRN-12-03) has 50–100- $\mu\text{m}$ -sized anhedral magnetite grains that are commonly associated with actinolite (Fig. 2h). The potassic granite intrusion (sample KRN-12-05) found underground within the mine (Westhues et al. 2016) has disseminated euhedral to anhedral magnetite grains that are  $<60$   $\mu\text{m}$  in size.

The Tuollavaara ore has subhedral to anhedral magnetite grains that range in size from 100 to 800  $\mu\text{m}$  (Fig. 3a). The host rock at Tuollavaara has disseminated magnetite with typically 1-mm-sized clusters of  $<100$ - $\mu\text{m}$ -sized grains that are anhedral (Fig. 3b). The Nukutus ore has subhedral to anhedral magnetite grains that range in size from 10 to 150  $\mu\text{m}$  with abundant apatite and interstitial actinolite  $\pm$  quartz, calcium carbonate, and biotite (Fig. 3c). The Rektorn ore is massive with interstitial calcite and quartz; BSE imaging revealed that approximately 60% of ore are lighter and therefore different in composition. Under reflected light, it was determined that the lighter BSE iron oxide is magnetite and the darker BSE iron oxide is hematite (Fig. 3d); both iron oxide phases were analyzed and differences in the chemistry are described in detail below. The Rektorn footwall host rocks contain abundant 1-

mm-sized magnetite grains with rims that are rich in inclusions of feldspar, biotite, and quartz (Fig. 3e).

### El Laco magnetite textures and associated minerals

The magnetite ore samples studied at the Laco Sur magnetite-apatite deposit are dominated by massive or anhedral magnetite; up to 2-mm-sized euhedral to subhedral grains can be found along the edges of void spaces (Fig. 4). Unlike the magnetite-apatite ore at Kiruna, the El Laco magnetite is generally not associated with other mineral phases and shows partial to extensive alteration to martite (i.e., pseudomorphic replacement of magnetite by hematite).

One of the samples from the upper levels of the ore body (ELL-14-04) consists primarily of massive magnetite or anhedral micrometer-sized grains of magnetite; there are abundant centimeter-sized elongated voids that are lined by 200–400- $\mu\text{m}$  euhedral magnetite crystals (Fig. 4a). In BSE images, the magnetite grains have porous inner cores that display chemical growth zoning and outer regions with no detectable chemical zoning. Under reflected light, the magnetite crystals show extensive alteration to kenomagnetite (nominally  $\text{Fe}^{2+}_{1-y}(\text{Fe}^{3+}_{1-2/3y})[\text{Y}]_{y/3}\text{O}_4$ ) and less extensively hematite along fractures (Ramanidou et al. 2008). Another sample from the upper levels of the ore body (ELL-14-05) consists primarily of spongy porous magnetite with centimeter-sized elongated voids that are lined with 200–600- $\mu\text{m}$  euhedral magnetite crystals (Fig. 4b). In BSE images, the magnetite crystals have concentric growth zoning with darker central regions. Under reflected light, hematite alteration can be seen along fractures in the magnetite and the edges of the magnetite. The magnetite from a magnetite vein in the lower level of the ore body (ELL-14-06) has 0.5–2-mm-sized magnetite grains that are euhedral along the edge of 0.5–1-cm-sized cavities, and the magnetite is anhedral elsewhere (Fig. 4c). In BSE images, the magnetite grains display a lighter core with darker portions that occurs along fractures and the grain rims. Under reflected light, the lighter BSE portions of the grain can be identified as magnetite and the darker portions are martite.

The andesite host rock has microphenocrysts of magnetite, 100–200  $\mu\text{m}$  in size, that are anhedral and contain trellis texture intergrowths of thin lamellae that in BSE images are visibly darker than the magnetite (Fig. 5a). Under reflected light, the lamellae were identified as ilmenite. The Láscar dacite has disseminated anhedral magnetite in  $<100$ - $\mu\text{m}$ -sized grains with local intergrown lamellae, visibly darker in BSE images, but this is not widespread (Fig. 5b, c). The lamellae in the Láscar dacite were identified as ilmenite with reflected light microscopy, a common texture found in titaniferous magnetite (Buddington and Lindsley 1964; Mehdilo and Irannajad 2010).

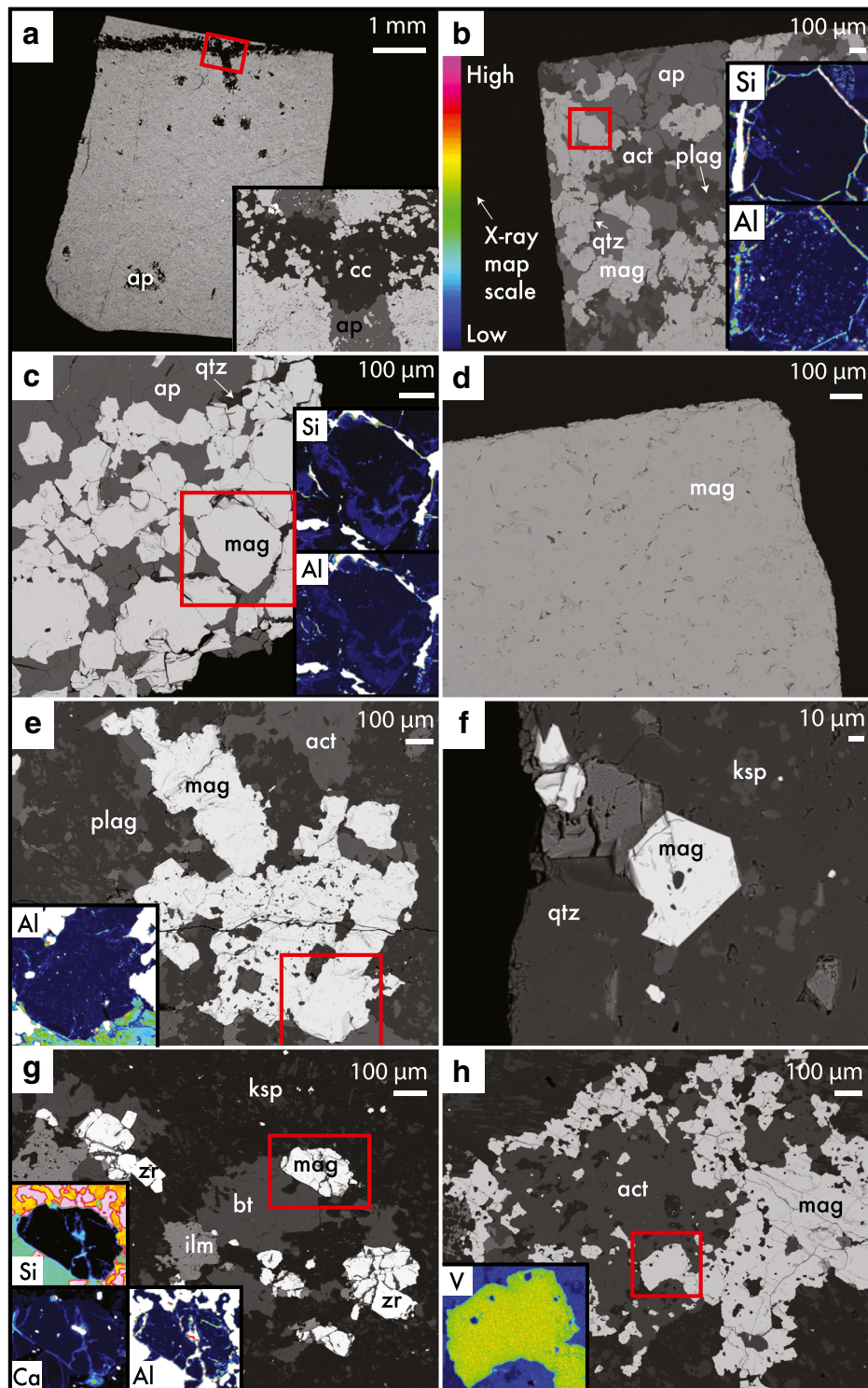


**Fig. 2** Back-scattered electron images and chemical X-ray maps of representative magnetite (*mag*) from the Kiirunavaara ore, host rocks, and associated intrusive rocks. **a** KRN-10-02 (D ore), massive magnetite with interstitial apatite (*ap*), and crosscutting calcium carbonate (*cc*) vein. **b** K-1 (D ore), subhedral magnetite grains with interstitial apatite, actinolite (*act*), plagioclase (*plag*), and quartz (*qtz*), zones of slight increases in Si and Al shown in X-ray map. **c** KRN-11-01 (D ore), subhedral magnetite similar to sample K-1, with correlating zones of increased Si and Al in the X-ray map. **d** K-2 (B ore), massive magnetite. **e** KRN-11-04 (FW), anhedral magnetite aggregate associated with actinolite; X-ray

map shows the spots of increased Al. **f** KRN-11-05 (HW), small euhedral-subhedral magnetite grain. **g** KRN-12-02 (syenite intrusive), small anhedral magnetite grains associated with zircon (*zr*), biotite (*bt*), and ilmenite (*ilm*) in a host of K-feldspar (*ksp*); X-ray map shows that the fractures in magnetite are filled with increased Ca, Si, and Al concentrations. **h** Anhedral magnetite associated with actinolite, rim of magnetite depleted in V relative to the core. Relative chemical variation scale for X-ray maps in **b**. Red boxes show the locations of BSE images or X-ray maps that are shown as insets



### Kiruna magnetite X-ray maps

Little chemical variation was observed in the X-ray maps for any of the Kiruna magnetite samples. The ore magnetite from the deposits in the Kiruna area display zones of elevated Al and Si that correlate with each other (see Figs. 2a, c and 3c). Many of the larger (>100  $\mu\text{m}$ ) ore and host rock magnetite grains display equally distributed spots of elevated Al throughout the grains that is not observed in the Si, V, Ca, or Ti X-ray maps (see Fig. 2a–e). These elevated Al spots are displayed in BSE images as darker spots (see Fig. 3a). The magnetite from the granite intrusive at Kiirunavaara (Fig. 2g) and the footwall magnetite at Rektorm that display elevated contents of Si, Al, Ca, and Ti can be found along structures that follow the typical shape of spinel exsolution lamellae

(Fig. 3e). The syenite sample of the Kiirunavaara mine revealed rims depleted in V (Fig. 2h). The Rektorm ore X-ray map has the most distinct chemical variations due to the presence of hematite that correlates to elevated Ti and V found in the zones darker in BSE (see Fig. 3d).

### El Laco magnetite X-ray maps

The ore magnetite-kenomagnetite crystal from ELL-14-04 that was mapped did not have a porous core that was observed in other grains from that sample and did not show any variation in chemistry. However, the adjacent grains in the X-ray map have porous cores which display elevated Si, Ca, and Al with growth zoning (Fig. 4a). The X-ray maps of the ELL-14-05 magnetite, with concentric growth zoning visible in BSE

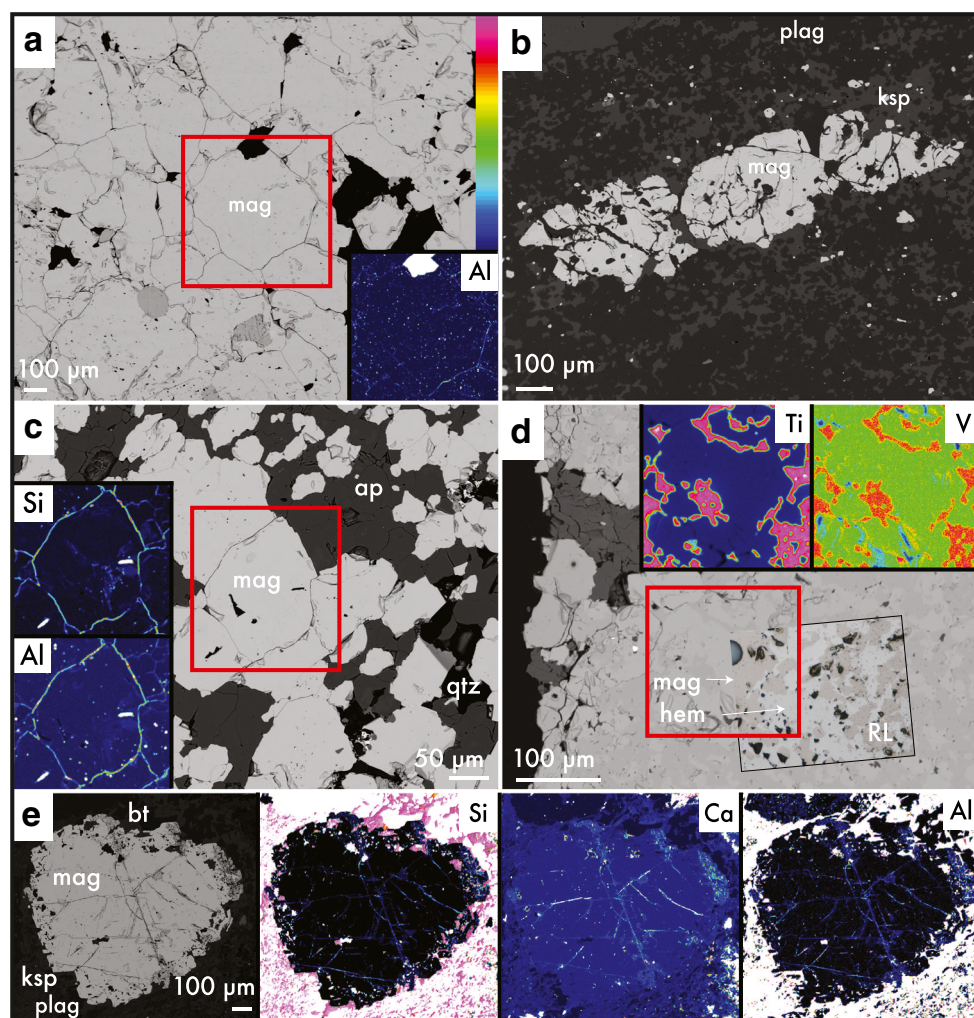


**Fig. 3** Back-scattered electron images and chemical X-ray maps of representative magnetite from the smaller magnetite-apatite ores and their host rocks in Kiruna. **a** TUV-10-01 (ore) equally distributed spots of high aluminum present in X-ray map are visible as darker spots in the BSE image. **b** TUV-10-03 (hanging wall), anhedral magnetite. **c** NUK-10-03 (ore), X-ray maps of Si and Al show a correlation. **d** REK-10-04 (ore), massive magnetite with dark hematite (*hem*) and brighter magnetite areas

in BSE correlating to *white* and *pink*, respectively, in reflected light (RL). The hematite has high Ti and V compared to the magnetite in the X-ray maps. **e** REK-12-02 (FW), correlating increases in Ca, Si, and Al are located along fractures in magnetite grain as seen in BSE image (*left*). See Fig. 2 caption for the previously mentioned mineral abbreviations. Relative chemical variation scale for X-ray maps in **a**. *Red box* surrounds the area of X-ray maps that are shown as *insets*

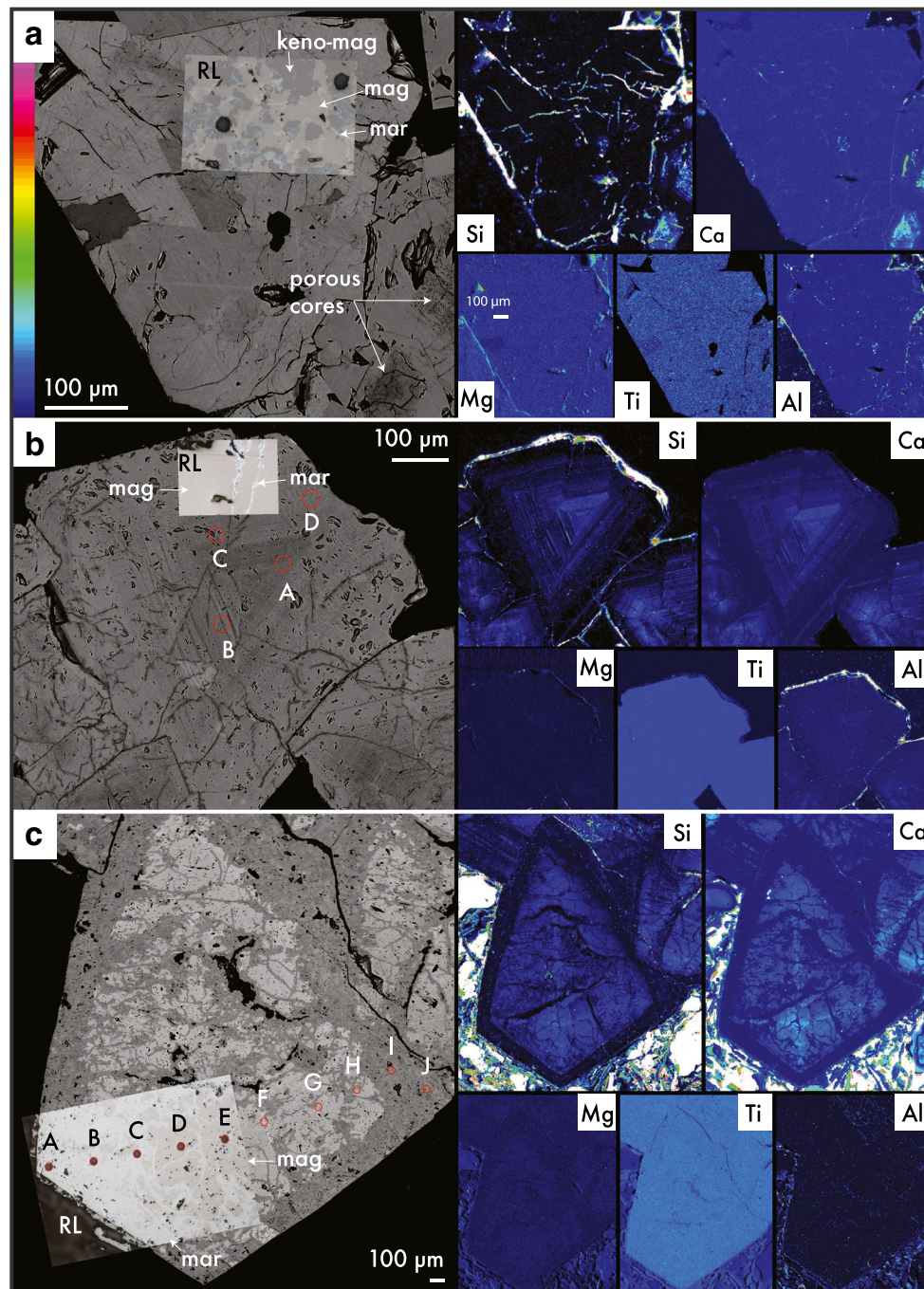


**Fig. 4** Back-scattered electron images and chemical X-ray maps of representative Laco Sur ore magnetite. **a** ELL-14-04, subhedral-euhedral magnetite grain with clear zoning in BSE imaging and no evident zoning in the X-ray maps for this grain. Adjacent grains with vuggy cores show the elevated growth zones of Si, Ca, and Al. Reflected light (RL) microscopy shows that the areas of the grain have been altered to keno-magnetite (*keno-mag*) and slight martite (*mar*) replacement along fractures. **b** ELL-14-05, subhedral-euhedral magnetite grains with clear growth zoning in the BSE image that correlates with the X-ray maps for Si, Ca, and Al; each element is elevated or depleted in the same layers with increasing concentrations towards the core. RL microscopy shows slight martite replacement along fractures. **c** ELL-

14-06, euhedral magnetite with clear zoning that correlates with increasing Si and Ca towards the core. RL microscopy shows that extensive replacement of the magnetite to martite has occurred, which correlates to very low trace element concentration in the X-ray maps. See Fig. 2 caption for the previously mentioned mineral abbreviations. Relative chemical variation scale for X-ray maps in **a**. Orange circles represent the LA-ICP-MS spot locations relevant to Fig. 6, and X-ray maps include the whole crystals shown in the BSE image. Direct comparisons in the zoning contrast in BSE cannot be made between each sample because the photographs were taken at different settings to optimize the chemical structure in the magnetite grains

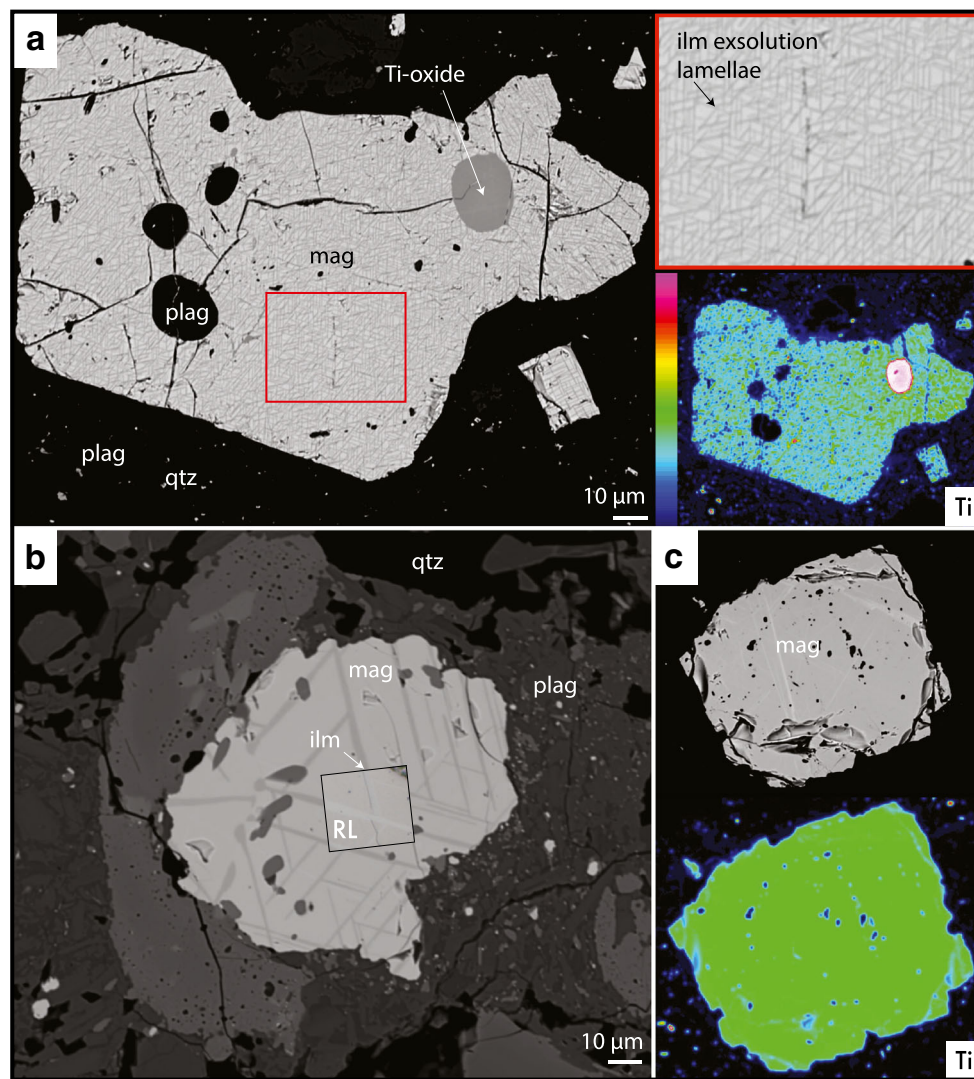


**Fig. 5** Back-scattered electron images and chemical X-ray maps of magnetite from the andesite host rock at El Laco volcano and the dacite sample from Láscar volcano. **a** ELL-14-02 (El Laco andesite), andesite with fine trellis textured ilmenite lamellae visible in BSE image and X-ray map for Ti; red box surrounds the magnified view of the exsolution

domain. **b, c** LAS-14-07 (Láscar dacite), ilmenite exsolution lamellae visible in BSE and RL are found in some grains (**b**) and are absent in others (**c**). See Fig. 2 caption for the previously mentioned mineral abbreviations. Relative chemical variation scale for X-ray maps in **a**

imaging, revealed increasing Si, Ca, and Al contents towards the core of the grain (Fig. 4b). Magnetite grains from a vein in the lower levels of the ore (ELL-14-06) display growth zoning in Si and Ca, and less obvious with Mg, with the highest concentrations in the central part of the grains. The martite (i.e., hematite)-replaced portions of the magnetite show lowest concentrations of trace elements (Fig. 4c). The El Laco andesite magnetite grain shows elevated Ti in the ilmenite exsolution lamellae that are visible in BSE imaging and reflected light microscopy (Fig. 5a). The Láscar dacite magnetite grain chosen for the X-ray map shows overall elevated Ti (Fig. 5c) compared to the El Laco magnetite.

### Trace element chemistry of Kiruna magnetite

The Fe content of magnetite for the ore, host, and intrusive rocks at Kiruna are slightly lower than the ideal stoichiometric value (72.4 wt% Fe) with EPMA results ranging from 69.4 and 70.8 wt% Fe (Table 2). The Fe contents for analyses on samples that were identified as hematite (REK-10-01 and REK-10-04) are distinctly lower than the magnetite and ranged from 63.8 to 68.5 wt% Fe. All of the magnetite grains from the Kiruna area, including the magnetite-apatite ore, host rocks, and related felsic intrusive rocks, are overall chemically homogeneous and contain low trace element concentrations

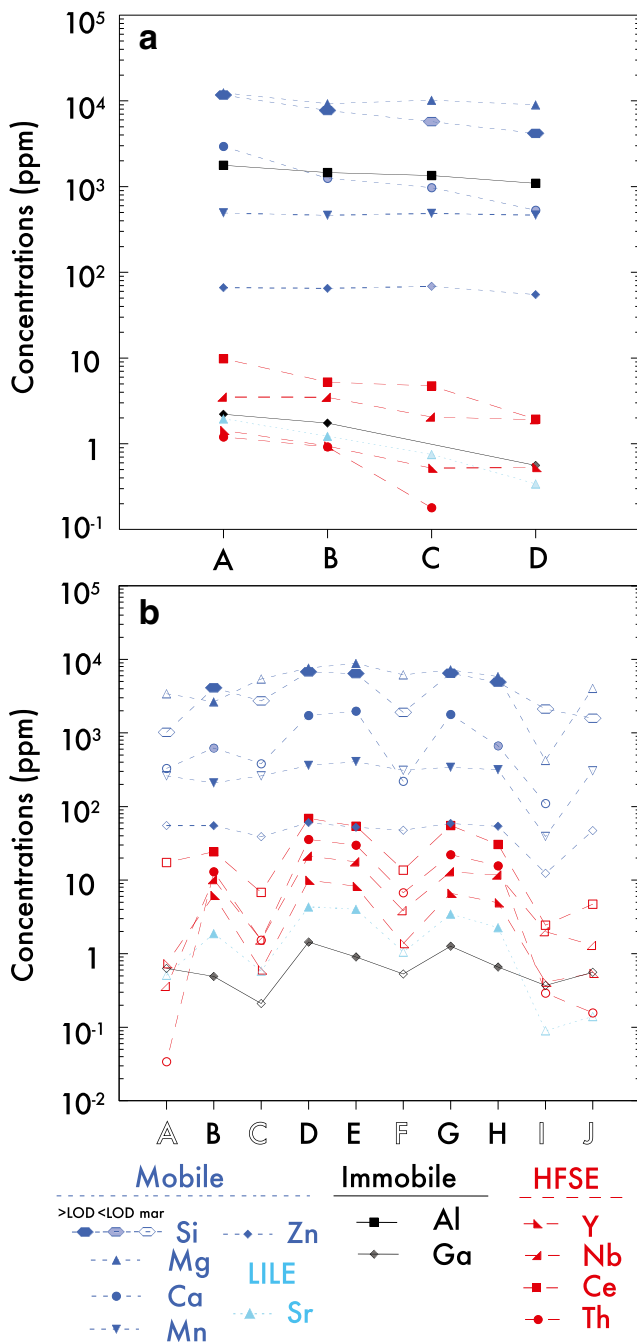


**Fig. 6** Trace element zoning patterns in magnetite grains from the Laco Sur magnetite ore. **a** ELL-14-05 ore sample (see Fig. 4c for the laser spot locations). **b** ELL-14-06 ore sample (see Fig. 5c for the laser spot locations). Faded symbols represent the analysis that is <LOD, and open symbols represent the analysis of martite (pseudomorphic replacement of magnetite to hematite). See text for details

(i.e., <500 ppm). The V concentrations, and locally the Si content, in the magnetite are generally higher than the other trace elements with concentrations around 0.1 and up to 0.2 wt%. The Ti contents are very low for magnetite with concentrations generally <50 ppm. The Kiirunavaara D-ore magnetite grains have higher Si and V contents

than the B-ore magnetite. The degree of alteration seems not to affect the chemical composition of the footwall magnetite at Kiirunavaara; both samples contain similar, and low, trace element concentrations. The hanging wall magnetite at Kiirunavaara has higher Si and lower V compared to the footwall magnetite. The magnetite from the syenite, aplite, and granite intrusive rocks at the Kiirunavaara deposit shows some variation in chemistry; particularly, the syenite magnetite, which has the highest Si content, and the aplite magnetite have the highest V content. The Nukutusvaara ore magnetite grains have higher Ti content than Kiirunavaara, Tuollavaara, and Rektorn. The Rektorn ore shows the most chemical variability visible in BSE, X-ray maps, and reflected light described earlier; trace element results confirm that the hematite contains elevated Ti and V and is depleted in Ni and Ga relative to the magnetite (see Fig. 7).

### Trace element chemistry of the El Laco magnetite

The Fe concentrations for magnetite in the Laco Sur ore are 67.25–70.4 wt% Fe. The magnetite grain that displays concentric growth zoning (ELL-14-05) showed decreasing Si, Ca (mobile elements), and Al (immobile element) towards the rim of the grain in the X-ray maps, and trace element analysis confirms this (Figs. 6a and 4b for the analysis locations). In addition, Mn; Ga; large-ion lithophile element (LILE); Sr; and high field strength elements (HFSE) Y, Nb, Ce, and Th follow a similar pattern, with a systematic decrease towards the rim. A euhedral magnetite grain from the magnetite vein referred to above (ELL-14-06) was analyzed 10 locations across the grain; this produced a chemical cross section of the grain (Figs. 6b and 4c for the spot locations). This cross section shows that the core is enriched in Mg, Si, and Ca, already detected in the X-ray maps (see Fig. 4c), as well as Mn, Ga, Sr, Y, Nb, Ce, and Th. Five of the analyses (A, C, F, I, and J) were done on magnetite that has been altered to martite, and these analyses show lower concentrations of each trace element that defines the zoning patterns in the magnetite. Other trace element concentrations, such as Ti, V, Cr, and Ni, show little to no variation between the pure magnetite and areas replaced by martite (see Figs. 7 and 9).

The host andesite at El Laco and the dacite from the Láscar volcano have lower Fe content with concentrations ranging from 59.4 to 65.6 wt% Fe and 56.8 to 61.4 wt% Fe, respectively. This is possibly due to the presence of unavoidable intergrowths of ilmenite lamellae and overall much higher Ti and other trace element concentrations. The andesite host rock magnetite at El Laco contains elevated concentrations of Al, P, Ti, V, Cr, Mn, Zn, Nb, and Ba compared to the ore magnetite, a similar pattern to

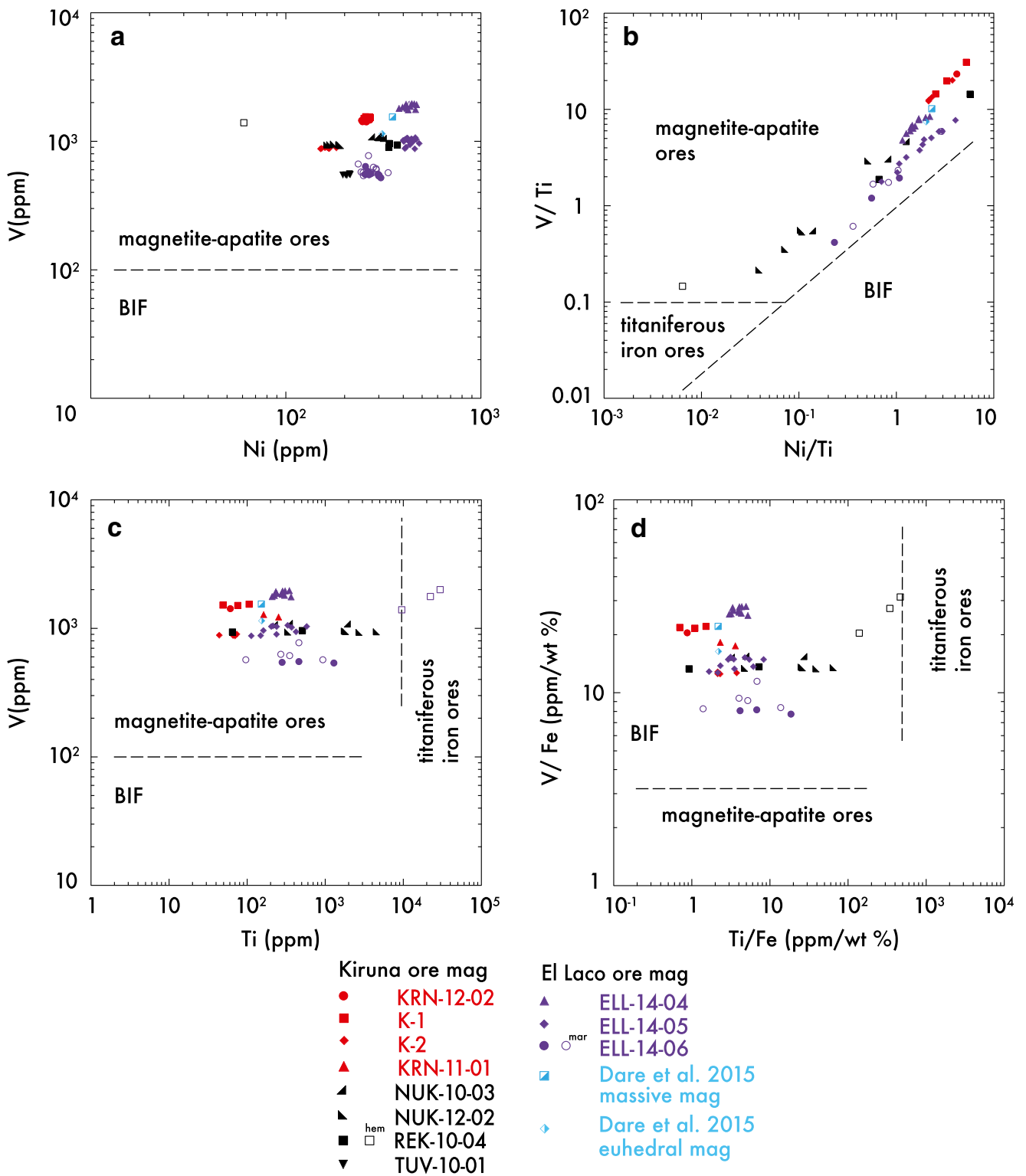


**Fig. 7** Magnetite discrimination plots by Loberg and Horndahl (1983) containing fields for magnetite-apatite ores and BIF (a–d) and titaniferous iron ores (b–d) with samples from this study plotted. **a** V (ppm) vs. Ni (ppm). **b** V/Ti vs. Ni/Ti. **c** V (ppm) vs. Ti (ppm). **d** V/Fe (ppm/wt%) vs.

Ti/Fe (ppm/wt%). The symbols used here for the ore magnetite are the same for the remaining figures in this paper. The open symbols represent the analysis of hematite or martite. See text for details

that described by Dare et al. (2015) (see Fig. 12). The dacite magnetite from Lásçar had the highest trace

element content with the addition of elevated Mg, Si, Ca, and Sn compared to the andesite magnetite.

### Mineral deposit-type discrimination diagrams

Loberg and Horndahl (1983) studied the geochemistry of magnetite in different types of iron ores, including magnetite-apatite, titaniferous, and BIF, including samples from the Kiruna and Bergslagen (southeast Sweden) regions and some samples from Iran and Chile. Fe, Ti, V, and Ni were used to create several discrimination plots. The V vs. Ni diagram (Fig. 7a) shows very homogeneous compositions of these two elements for each individual sample, but there are significant variations between samples from each locality and

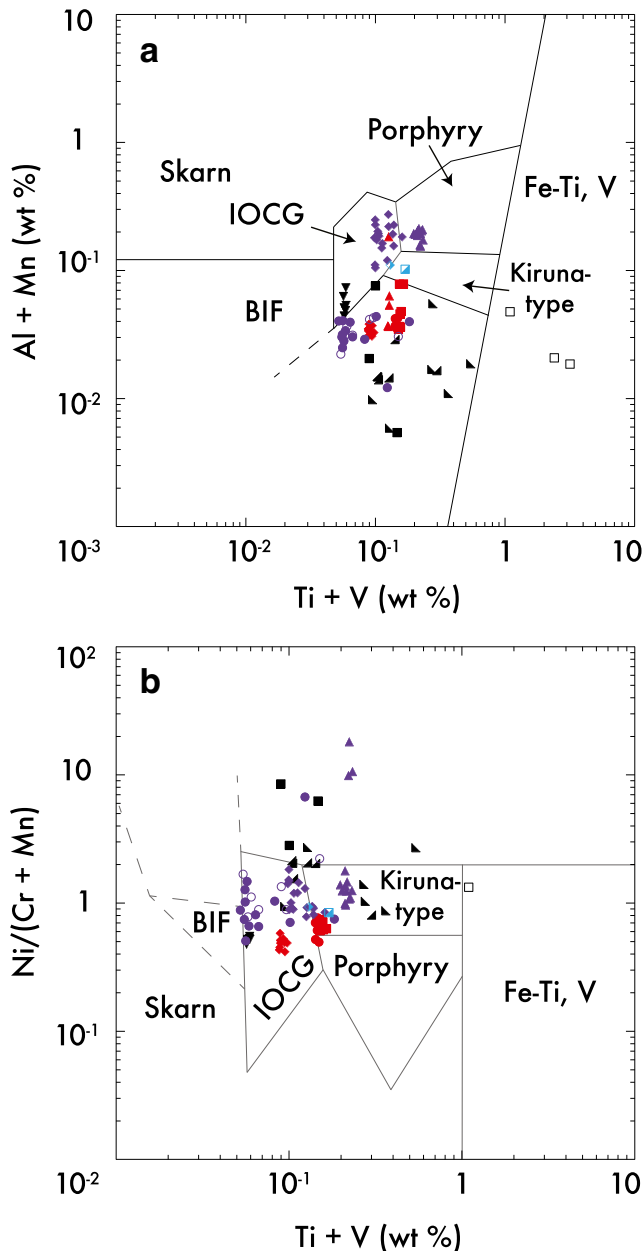


**Fig. 8** Magnetite discrimination plots for various ore deposit types by Dupuis and Beaudoin (2011) and modified by Nadoll et al. (2014) with samples from this study plotted. **a** Al + Mn (wt%) vs. Ti + V (wt%). **b** Ni/(Cr + Mn) vs. Ti + V (wt%). See text for details

between El Laco and Kiruna samples. In contrast, the Ti concentrations are rather heterogeneous and vary considerably even within each sample (Fig. 7b–d). Distinct chemical variations between the Kiirunavaara ore (lowest Ti contents), the Per Geijer ores near Kiruna (highest Ti concentrations), and the El Laco ores are observed. The hematite from the Rektorn ore and the martite-replaced portions of the El Laco magnetite have been plotted here and on the following diagrams to illustrate how the hematite compositions compare to the magnetite compositions for the discussion; we do not, however, suggest that hematite can be used on these diagrams to determine its environment of crystallization.

Dupuis and Beaudoin (2011) also proposed several empirical discrimination diagrams for magnetite from various deposit types including BIF, IOCG, magnetite-apatite (Kiruna-type), porphyry-Cu, skarn, and Fe-Ti-V-layered mafic intrusion deposits (Fig. 8). The two diagrams are based on Al + Mn + Ca (wt%) (Fig. 8a) and Ni/(Cr + Mn) (Fig. 8b) on the y axis vs. Ti + V (wt%) on the x axis. In these plots, the field of the Kiruna-type deposits was based on the analysis of magnetite from seven different magnetite-apatite locations around the world, including Kiruna and El Laco (Dupuis and Beaudoin 2011). It should be noted that the samples chosen from Kiruna and El Laco are different to those used in the present study. These diagrams are suggested for usage during mineral exploration to fingerprint different styles of mineralization using magnetite chemistry. We chose the version of the first diagram (Fig. 8a) modified by Nadoll et al. (2014), who

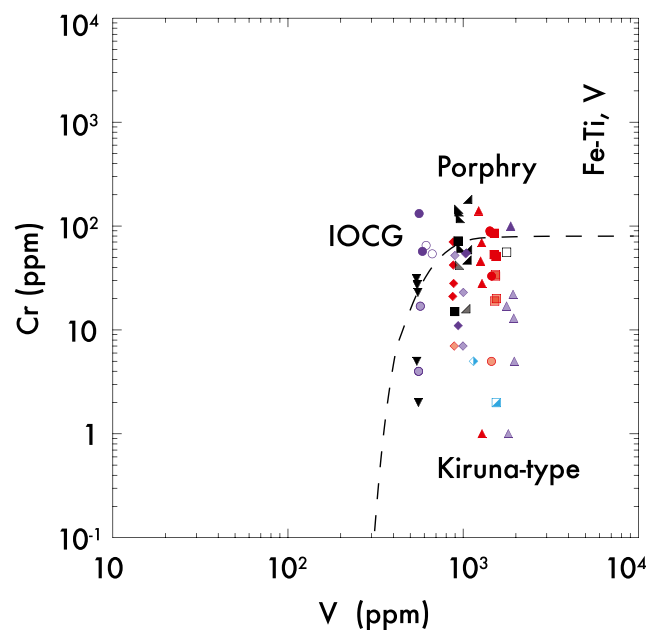


**Fig. 9** Cr vs. V plot discriminating Kiruna type from other ore deposit proposed by Knipping et al. (2015). Many of the magnetite grains from the Kiruna and El Laco magnetite-apatite ores in this study contain higher Cr concentrations than suggested in this diagram. The faded symbols represent the analysis of Cr that is <LOD. See text for details

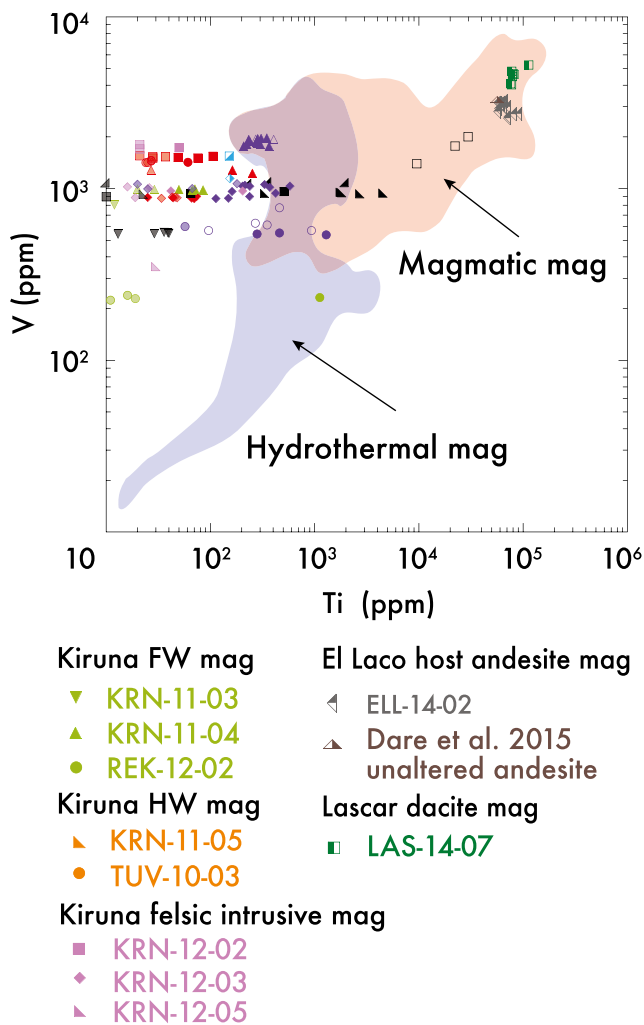


**Fig. 10** V vs. average concentrations for this study d magmatic magnetite fields drawn by Knipping et al. (2015). The plot suggests overall higher Ti and V concentrations in igneous magnetite with considerable overlap in Ti and V chemistry between hydrothermal and igneous magnetite. The *symbols* used for magnetite samples of the host rock and related intrusive bodies are the same for the remaining figures in this paper. The *faded symbols* here represent the analysis of Ti that is <LOD. See text for details

eliminated Ca from the y axis component, because plotting with or without Ca made little difference where our data plotted because the Ca contents are low or below the LOD.

In Fig. 8a, the majority of the Kiruna and El Laco magnetite analyses from the present study have very low Ti concentrations and therefore do not plot within the proposed Kiruna field. Magnetite from the Rektorn ore with elevated Ti plots within the Fe-Ti, V deposit field. Magnetite from the stratabound ore of El Laco plots non-uniquely in the IOCG and porphyry copper fields, situated above and to the left of the Kiruna-type field.

In Fig. 8b, about one third of the magnetite-apatite ore analyses plot within the Kiruna-type field but the majority plot within the IOCG field. The Ti-rich hematite from the Rektorn

ore is distinct from the magnetite and plots within the Fe-Ti, V deposit field. The Ti-poor magnetite from the Rektorn ore plots above the IOCG and Kiruna-type fields.

Knipping et al. (2015) presented a discrimination diagram to distinguish Kiruna-type deposits from porphyry; IOCG; and Fe-Ti, V deposits based on the Cr and V contents of the magnetite (Fig. 9). The Kiruna-type deposits were defined as having low Cr content (<~100 ppm) and high V content (>~500 ppm). Some of the magnetite analyses from the Kiruna and El Laco magnetite-apatite ores in this study have higher Cr content than previously reported (Dare et al. 2015) and plot above the Kiruna-type field with similar Cr and V contents as magnetite from IOCG and porphyry deposits.

**Magmatic vs. hydrothermal magnetite discrimination diagrams**

Nadoll et al. (2015) proposed using the concentrations of Ti and V in magnetite to distinguish between hydrothermal and magmatic magnetite (Fig. 10). The justification for this diagram is that Ti and V are often found in high concentrations within magmatic magnetite and low concentrations within hydrothermal magnetite (Nadoll et al. 2015; Knipping et al. 2015). Knipping et al. (2015) used this diagram as well to support their magmatic-hydrothermal model for the formation of magnetite-apatite deposits and drew magmatic and

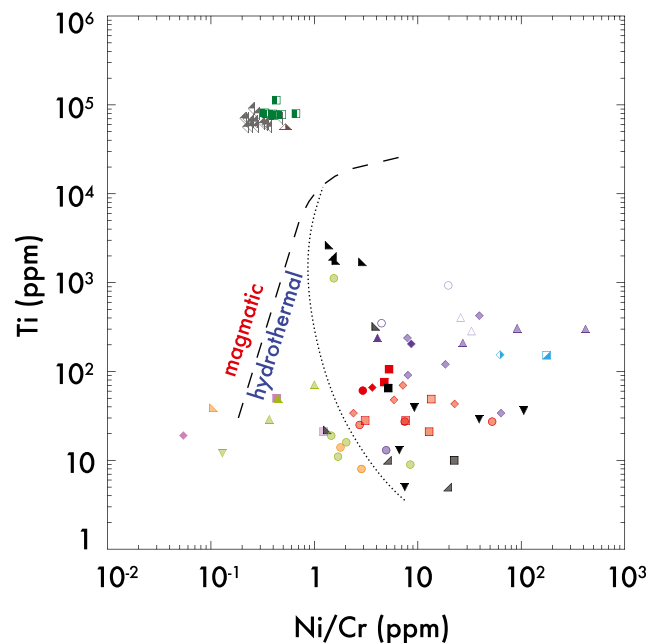


**Fig. 11** Samples from this study plotted on the Ti vs. Ni/Cr plot proposed by Dare et al. (2014) to discriminate between magmatic and hydrothermal environments for magnetite formation. The majority of the magnetite data from Kiruna and the ore magnetite from El Laco had either Ni, Cr, or Ti < LOD, and these analysis are plotted here as *faded symbols*. The *dotted line*, placed in this study, separates the host and intrusive magnetite in Kiruna from the ore magnetite. See text for details

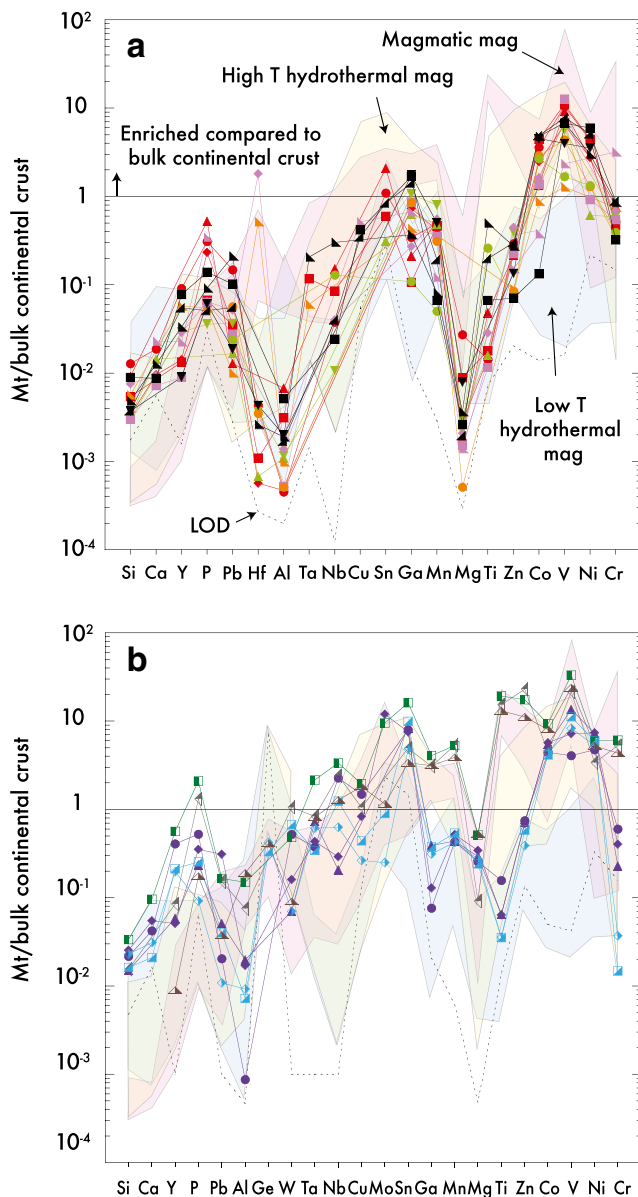


**Fig. 12** Samples from this study on a multi-element variation diagram proposed by Dare et al. (2014) showing trace elements in magnetite normalized to bulk continental crust from Rudnick and Gao (2003). Zones showing the proposed compositional patterns of magnetite from magmatic (pink), high-temperature (yellow), and low-temperature (blue) hydrothermal environments are shown. Each zone was adjusted in this study to accommodate elements that were not analyzed. See text for details

hydrothermal fields using magnetite data from Nadoll et al. (2015). This is essentially the same plot used by Loberg and Horndahl (1983) to describe magnetite from magnetite-apatite deposits vs. BIF and titaniferous iron ores (see Fig. 7c), though used here to describe magnetite from different environments.

In Fig. 10, magnetite data from the magnetite-apatite ores are plotted with the addition of the host rock magnetite to evaluate the fields drawn by Knipping et al. (2015). Most of the Kiruna magnetite data in the present study do not plot within the magmatic, hydrothermal, or overlapping magmatic-hydrothermal fields. The magnetite from the Kiirunavaara ore and host rocks has very low Ti concentrations that are at or below LOD and plot to the left of the overlapping magnetite-apatite field. The footwall magnetite at Rektorn plots within the hydrothermal magnetite field. The stratabound ore magnetite at El Laco plots within the overlapping magnetite-apatite field or to the left of this field. The host andesite magnetite at El Laco and the Láscar dacite magnetite, both with high Ti and V concentrations, plot at the far top right of the magmatic field.

Dare et al. (2014) proposed an empirical discrimination diagram of Ti vs. Ni/Cr that shows that there is a distinct chemical difference between magnetite that precipitated from hydrothermal fluids and magnetite that crystallized from a magmatic melt (Fig. 11). Most of our magnetite data, including the host rock magnetite data for Kiruna, had one or more of the elements required for this plot below LOD. The Kiruna and Laco Sur ore magnetite as well as most of the Kiruna host rock and related intrusive magnetite, which occurs in igneous rocks, plot within the hydrothermal magnetite field proposed by Dare et al. (2014) due to the low Ti and Cr contents of the magnetite. However, magnetite from the Kiruna host rocks and related intrusive rocks show a distinctly lower Ni/Cr ratio compared magnetite from the Kiruna and El Laco ore.

Trace element variations for magnetite were plotted on a multi-element diagram proposed by Dare et al. (2014) that was modified in this present study to leave out trace elements not commonly found in magnetite and not measured in this study (e.g., Zr, Ge, W, Sc, and Mo from the Kiruna analyses and Zr, Hf, and Sc from the El Laco analyses) (Fig. 12). Elements are normalized to the bulk continental crust data from Rudnick and Gao (2003). This diagram shows there to be distinct trace element chemical patterns between magnetite from a magmatic origin and from magnetite that could be from a high-T or low-T hydrothermal origin. Magmatic magnetite patterns from Dare et al. (2014) are based on data from the El Laco andesite and the Bushveld complex as well as magnetite from I-type granite. The high-temperature hydrothermal (500–700 °C) region was defined using analytical results for magnetite from nine different IOCG deposits. The low-temperature hydrothermal zone (<500 °C) is based on magnetite from iron-rich skarns,



Ag-Pb-Zn veins, and BIFs. Average results from each magnetite sample in the present study were used for this plot (ESM Table 3A); this made the diagram easier to read and interpret.

The trace element patterns for the magnetite-apatite ores at Kiruna are most similar to the high-temperature hydrothermal magnetite (Fig. 12a). Magnetite within the host and intrusive rocks in Kiruna for the most part follows a similar trace element pattern to the ore magnetite, in the high-temperature hydrothermal zone, though with overall lower trace element concentrations than the ore magnetite. None of the host magnetite at Kiruna resembles the proposed magmatic trend even though they are hosted in volcanic rocks, except peaks in Hf in magnetite from the Kiirunavaara hanging wall and the syenite sill in the footwall at Kiirunavaara.

The trace element patterns for the Laco Sur ore magnetite show similar trends as the high-temperature hydrothermal pattern, with high Mg trending into the magmatic field and low Ga trending into the low-temperature hydrothermal field (Fig. 12b). The andesite host rock magnetite at El Laco and the Lásçar dacite magnetite follow the magmatic magnetite trend. All magnetite from El Laco and Lásçar analyzed in the present study, including the andesite and dacite magnetite, show higher concentrations of Si, Ca, Y, and P than with the volcanic dacite magnetite containing the highest concentrations of these elements.

## Discussion

The trace element geochemistry of magnetite depends on availability of chemical elements and the ability of the host mineral to incorporate the trace element in its structure, which can depend on variables such as the temperature, redox state or the partition coefficient ( $K_D$ ) of magnetite, and coexisting mineral phases. Also, drop in the temperature or fluctuating conditions can lead to exsolution of separate phases, which also has to also be taken into account. Furthermore, the accurate use of discrimination diagrams should also exclude the presence of nanoinclusions, which cannot always be removed during the LA-ICP-MS analyses and data reduction.

### The use of mineral deposit-type discrimination diagrams

The Loberg and Horndahl (1983) diagrams (see Fig. 7) effectively plot the magnetite-apatite ores within the appropriate fields. These diagrams contain very broad

discrimination fields, which accounts for the chemical variation observed in the ore magnetite.

The Dupuis and Beaudoin (2011) diagrams (see Fig. 8) have narrow discrimination fields. The magnetite-apatite data from this study do not plot within the proposed Kiruna-type discrimination field and overlapped significantly with other deposit types such as IOCG and porphyry-Cu. There is too much overlap in magnetite chemistry from the Kiruna-type, magnetite-apatite mineralization and the other types of deposits for this diagram to work effectively. For instance, if these diagrams were to be used in mineral exploration using magnetite as an indicator mineral, it would be impossible to distinguish magnetite sourced from magnetite-apatite ores from magnetite from IOCG or Cu-porphyry deposits. Thus, and based on the results from the present study, the Kiruna field needs to be significantly modified or removed from the diagram. Since many of the magnetite-apatite ore analyses plot within the IOCG field, this could have implications that magnetite-apatite ores form hydrothermally in a manner similar to genetic models suggested for IOCG deposits or, alternatively, could reveal a flaw in the rationale for these diagrams.

The Knipping et al. (2015) Cr/V discrimination diagram has a field drawn for Kiruna-type deposits with distinctly lower Cr content from porphyry; IOCG; and Fe-Ti, V deposits and higher V content than IOCG (see Fig. 9). The rationale behind the Kiruna-type field in this diagram is that higher V content relates to the high temperatures. Low Cr content of Kiruna-type magnetite is explained by its high  $K_D$  into augite prior to crystallization of magnetite or, and deemed more likely, the high mobility of  $\text{Cr}^{6+}$  into oxidized fluids that transported Cr out of the magnetite-apatite ore-forming system. As mentioned above in the results, several of the magnetite analyses from the Kiruna and El Laco ores in this study have higher Cr contents than previously reported for those localities (Dare et al. 2015). Assuming that the rationale behind the diagram is valid, higher Cr content observed in the ore magnetite in the present study suggests that Cr and possibly other elements that are mobile in hydrothermal fluids, such as Si, Ca, and LILE, were not transported out of the system but were incorporated into the magnetite.

### The use of magmatic vs. hydrothermal magnetite discrimination diagrams

Nadoll et al. (2015) and later Knipping et al. (2015) used V and Ti concentrations to discriminate between magmatic and hydrothermal magnetite (see Fig. 10). Based on

the magnetite data from the present study, and those of Velasco et al. (2016), it is clear that magnetite from the magnetite-apatite deposits has extremely variable V and Ti concentrations. Thus, many of the magnetite samples here plot outside the fields on this diagram, questioning the integrity of the plot. Dare et al. (2014) proposed another diagram that discriminates between magmatic and hydrothermal magnetite using Ti and Ni/Cr concentrations (see Fig. 11). Although magnetite from the magnetite-apatite ore plots within the hydrothermal magnetite field, this does not necessarily verify that they formed hydrothermally. A recent study by Velasco et al. (2016) showed that massive magnetite from the stratabound ore, and the disseminated magnetite related to the early alkaline-calcic alteration, and of undisputable hydrothermal origin, plot in both the magmatic and hydrothermal fields. Probably, these empirical diagrams are too simple to distinguish and the Ti and Ni/Cr ratios do not only depend on the precipitation from silicate or aqueous fluids or need additional constraints and/or adjustments.

Magnetite that crystallized from a melt of unique composition may contain lower Ti concentrations than is normal for igneous magnetite. The multi-element variation diagrams proposed by Dare et al. (2014) have fields that overlap significantly with each other, and none of the analyses from the present study plot perfectly within one field, leaving ambiguity regarding the utility of that diagram (see Fig. 12). Furthermore, it must be considered that it is not possible to directly compare the trace element patterns between immiscible melts, such as a silicate melt and a presumable iron-rich melt, since during phase separation, the  $K_D$  irregularly distributes the elements between them.

### Magnetite chemistry at Kiruna

The magnetite studied from the Kiruna magnetite-apatite ores is generally very homogenous. It is suggested here that the original trace element chemistry of the magnetite in the Kiruna ore and their host rocks were affected by subsequent hydrothermal alteration and metamorphism. The rocks at Kiruna have undergone widespread hydrothermal alteration (Frietsch 1978; Romer et al. 1994; Westhues et al. 2016) and up to greenschist facies metamorphism (Bergman et al. 2001), where widespread recrystallization of magnetite can occur (Dahl 1979). The X-ray maps of the Kiruna magnetite grains revealed areas of increased Si and Al that often are correlated with each other. These zones are blotchy and random and could likely be a result of metasomatic alteration. The high-Al domains are most prominent in the larger

grains of the ore, and footwall magnetite could be nanoinclusions of an Al-rich mineral or may also be the result of metasomatic alteration.

Hydrothermal titanite is widespread in the Kiruna ore (Romer et al. 1994; Storey et al. 2007) and indicates that the hydrothermal fluids contained Ti. Titanite has been dated to be just younger, though with overlapping error ( $1876 \pm 9$  Ma, U-Pb TIMS (Romer et al. 1994);  $1876 \pm 17$  Ma, U-Pb SIMS (Westhues et al. 2016)) than the volcanic rocks around Kiirunavaara ( $1890 \pm 90$  Ma, Sm-Nd isochron (Cliff et al. 1990);  $1884 \pm 4$  to  $1880 \pm 3$  Ma, U-Pb SIMS (Westhues et al. 2016)). Together with in situ dating of hydrothermally influenced zircon from the altered host rocks and ore ( $1876 \pm 7$  and  $1874 \pm 7$  Ma, respectively), Westhues et al. (2016) suggested that the titanite ages reflect the metasomatic alteration overlapping with the ore formation. The hematite portions of the Rektorn ore have considerable higher Ti content than the magnetite, again suggesting that the alteration fluids contained appreciable amounts of Ti.

Although the magnetite chemistry of the Kiruna rocks are very similar in most elements (see Figs. 10 and 12), the Ni/Cr vs. Ti plot after Dare et al. (2014) (see Fig. 11) revealed a distinct difference in the Ni/Cr of the magnetite from the magnetite-apatite ores and the host rocks/related felsic intrusive rocks. The latter have a more similar Ni/Cr content as the El Laco host rocks but with lower Ti concentrations. This may suggest that before alteration of the host rocks, primary magnetite may have had a similar composition to the magnetite from volcanic rocks in Chile. Also, the magnetite ore in Kiruna likely formed with low trace element concentrations, similar to the El Laco ore magnetite; therefore, alteration of the trace elements is not so apparent as with the host rock magnetite. Because the chemistry of the primary magnetite may have been altered, it is difficult to draw any conclusive arguments on how the magnetite-apatite ores formed through the utilization of empirical magnetite discrimination diagrams.

### Magnetite chemistry at El Laco

The magnetite from El Laco is much younger than at Kiruna and has not been affected by metamorphism, but most of it likely has undergone various degrees of hydrothermal alteration (Tornos et al. 2016), made evident by replacement of magnetite by keno-magnetite and martite. There are clear chemical differences at El Laco in the magnetite ore and magnetite from the andesite host and the dacite sample from the nearby Láscar volcano. The andesite and dacite samples have similar trace ele-

ment chemistry with signatures that plot as igneous magnetite on proposed discrimination diagrams (see Figs. 10, 11, and 12) and have clear exsolution textures common in Ti-rich magmatic magnetite crystallized in hot and reduced settings (Mehdilo and Irannajad 2010). The Lásca dacite magnetite has elevated trace element concentrations compared to the El Laco andesite magnetite. This may indicate that the source melt of the volcanic rocks at Lásca has a different composition from the El Laco volcanic rocks or certain physicochemical parameters were different such as lower  $fO_2$  of the melt at Lásca during magnetite crystallization.

The ore magnetite at El Laco shows clear zonation patterns in BSE and X-ray maps, which have also been described by previous authors (Fig. 4) (e.g., Velasco and Tornos 2012; Dare et al. 2015; Velasco and Tornos 2012). The centers of the magnetite crystals show elevated concentrations of Mg, Si, Ca, and LILE (Fig. 6) compared to the outer regions; these elements are considered to be mobile in hydrothermal environments (Dare et al. 2014; Nadoll et al. 2014). However, the cores also show elevated concentrations of Al and Ga, which are considered generally immobile in hydrothermal fluids as well as HFSE (Y, Nb, Ce, and Th), which are incompatible during partial melting but not as readily mobile in hydrothermal fluids (McCulloch and Gamble 1991; Blake 1992). Also, the ore magnetite were reported as being “enriched” in elements that are highly mobile in hydrothermal fluids, though concentrations of these elements are not higher than was detected in the unaltered andesite magnetite or the Lásca dacite magnetite (see Fig. 12. and ESM).

Looking closely at the zoning chemistry of the El Laco ore magnetite, a combination of incompatible elements, compatible elements, LILE, and HFSE have correlated concentrations (i.e., they are all found either elevated or depleted in the same layers) (see Fig. 4). If the El Laco ores formed through metasomatic replacement of the andesite host rock, it would not be expected that the combination of elements that produced the element zoning would behave the same, since these elements do not have the same mobility in hydrothermal fluids. Dare et al. (2014) describes iron-rich skarn magnetite as having element concentrations and euhedral zoning similar to the El Laco magnetite. However, the elements that define growth zones in the iron-rich skarn magnetite are not enriched and depleted in the same layers, suggesting quick changes in the composition of the igneous/aqueous fluid pulses that crystallized the magnetite. Also, elements such as V and Ni are zoned in the iron-rich skarn magnetite (Dare et al. 2014), and this is not

observed in the El Laco magnetite, suggesting that not all elements were fluctuating during magnetite growth, as would be the case during growth from hydrothermal fluids.

The type of hydrothermal alteration, the mass balance relationships, and the fluid inclusion and isotope results suggest that purely hydrothermal models and replacement of the host lavas at very shallow depths are geologically unrealistic (see Tornos et al. 2016). It should also be noted that spherical to spheroidal magnetite particles have been described from more friable ore than the samples used in the study, textures that are best explained by rapid cooling of an iron-rich melt (Henríquez and Martín 1978; Nyström et al. 2016).

Thus, the chemistry of the magnetite at El Laco can be explained by magnetite crystallizing from an iron-rich melt that is initially enriched in the elements involved in the zonation pattern with periodic replenishment from the source melt during magnetite growth with less replenishment over time or, and more likely, the crystallization of magnetite during fluctuating redox conditions ( $fO_2$ ), fluid content, and temperature of the melt. The interpretation here is that the iron-rich melt became more oxidized as it moved closer to the surface. In an oxidized system, there is an increase of  $Fe^{3+}$ , which primarily occupies the octahedral sites in magnetite, inhibiting the incorporation of other elements that were present in the iron-rich melt (Buddington and Lindsley 1964).

## Conclusions

After a critical evaluation of empirical magnetite discrimination diagrams using newly obtained data on the trace element composition of magnetite from precisely known geographic and geologic locations (encompassing the Kiruna and El Laco magnetite-apatite ores and their associated hydrothermally altered host rocks), the following conclusions can be drawn in respect of a hydrothermal or magmatic origin for magnetite:

- 1) Only the earlier diagrams by Loberg and Horndahl (1983), with very broad discrimination fields, effectively display magnetite from the magnetite-apatite ores in this study within the appropriate field. The more recent discrimination diagrams proposed by Dupuis and Beaudoin (2011) and Knipping et al. (2015) do not constrain the data from this study in the appropriate Kiruna-type field and indicate that magnetite from Kiruna-type deposits have compositions similar to other types of deposits; thus,

these diagrams are not effective as discrimination diagrams.

- 2) The Cr content from Kiruna-type magnetite reached higher concentrations than previously reported by Knipping et al. (2015); this calls into questions the validity of the Cr-V plot as well as conclusions drawn from using this plot to support the genetic model for magnetite-apatite deposits that is proposed by these authors.
- 3) The magmatic vs. hydrothermal discrimination diagram for magnetite by Knipping et al. (2015) needs modification as many of the data from the present study do not plot within either of the proposed fields.
- 4) The magmatic vs. hydrothermal magnetite diagram by Dare et al. (2014) had limited use because most of the data collected had non-detectable Cr, Ni, or Ti concentrations. The data below LOD, however, had to be plotted in order to evaluate this diagram. The indisputably igneous magnetite (e.g., El Laco andesite and Láscar dacite) effectively plotted within the magmatic magnetite field. The magnetite-apatite ores from El Laco and Kiruna and host rock magnetite at Kiruna all plot within the hydrothermal field. The host rock magnetite has distinctly lower Ni/Cr ratio than magnetite from the magnetite-apatite ores.
- 5) The multi-element variation diagrams for magnetite proposed by Dare et al. (2014) only work for Kiruna-type magnetite if the ores are actually of hydrothermal origin.

After reviewing the chemistry and textures of the magnetite from the Kiruna and El Laco magnetite-apatite ores and their host rocks, the following conclusions can be made:

- 1) It is likely that the magnetite at Kiruna is largely influenced by subsequent metamorphism and/or metasomatic alteration. Whether the magnetite-apatite ores, which show hydrothermal signatures on the diagrams discussed above, originated from hydrothermal fluids or formed later through post-ore metamorphic or metasomatic alteration cannot be determined using magnetite chemistry alone.
- 2) The magnetite from magnetite-apatite ores at El Laco have chemical zonations that appear similar to Fe-rich skarns (Dare et al. 2015), though there are very distinct differences in the zonation patterns. Observations of the chemical zonation patterns in the El Laco magnetite that do not correlate with iron-rich skarn magnetite include (a) the El Laco ore magnetite has zonations of compatible LIL and HFS elements that are all elevated or depleted in the same crystal layers and (b) some compatible elements are homogenous across the

magnetite grains (i.e., V and Ni). With these observations, we propose that the magnetite at El Laco is indicative of having crystallized from a volatile-rich, iron-oxide melt that was fluctuating in physiochemical conditions rather than from replacement of the host rocks by pulses of hydrothermal fluids.

**Acknowledgements** We would like to thank the Natural Sciences and Engineering Research Council of Canada (NSERC) discovery grant to JMH. The contribution of FT has been funded by the project SEIDI 2014 CGL2014-55949-R. Thanks to Luossavaara-Kiirunavaara Aktiebolag (LKAB) and Compañía Minera del Pacífico (CMP) for the help in logistics and permission to sample and granting access to the mine sites. We thank the reviewers (P. Williams and N. Oliver) for the thorough and constructive criticism of the original manuscript and to P. Williams for the comments on the revised manuscript. Thanks also to B. Lehmann for his review and editorial additions and handling of this paper.

## References

- Alva-Vadivia LM, Rivas ML, Goguitchaichvili A, Urrutia-Fucugauchi J, Gonzalez JA, Morales J, Gómez S, Henríquez F, Nyström JO, Naslund RH (2003) Rock-magnetic and oxide microscopic studies of the El Laco ore deposits, Chilean Andes, and implications for magnetic anomaly modeling. *Int Geol Rev* 45:533–547
- Barton MD, Johnson DA (1996) Evaporitic-source model for igneous-related Fe oxide-(REE-Cu-Au-U) mineralization. *Geology* 24:259–262
- Barton MD, Johnson DA (2004) Footprints of Fe-oxide(-Cu-Au) systems. SEG 2004: predictive mineral discovery under cover. Centre for Global Metallogeny, *Spec Pub* 33:112–116
- Bergman S, Kubler L, Martinsson O (2001) Description of regional geological and geophysical maps of northern Norrbotten County (east of the Caledonian orogen). *Sveriges Geologiska Undersökning* 56: 110
- Blake KL (1992) The petrology, geochemistry and association to ore formation of the host rocks of the Kiirunavaara magnetite-apatite deposit, northern Sweden. PhD thesis. University of Wales College of Cardiff, 307 pp.
- Buddington AF, Lindsley DG (1964) Iron-titanium oxide minerals and synthetic equivalents. *J Petrol* 5(2):310–357
- Cliff RA, Rickard D, Blake K (1990) Isotope systematics of the Kiruna magnetite ores, Sweden: part 1. Age of the ore. *Econ Geol* 85:1770–1776
- Dahl PS (1979) Comparative geothermometry based on major-element and oxygen isotope distributions in Precambrian metamorphic rocks from southwestern Montana. *Am Mineral* 64:1280–1293
- Dare SAS, Barnes S-J, Beaudoin G, Méric J, Boutroy E, Potvin-Doucet C (2014) Trace elements in magnetite as petrogenetic indicators. *Mineral Deposita* 49:785–796
- Dare SAS, Barnes S-J, Beaudoin G (2015) Did the massive magnetite “lava flows” of El Laco (Chile) form by magmatic or hydrothermal processes? New constraints from magnetite composition by LA-ICP-MS. *Mineral Deposita* 50:607–617
- Dupuis C, Beaudoin G (2011) Discriminant diagrams for iron oxide trace element fingerprinting of mineral deposit types. *Mineral Deposita* 46:319–335
- Dymek RF, Owens BE (2001) Petrogenesis of apatite-rich rocks (nelsonites and oxide-apatite gabbro-norites) associated with massif anorthosites. *Econ Geol* 96:797–815

- Edfelt A, Armstrong RN, Smith M, Martinsson O (2005) Alteration paragenesis and mineral chemistry of the Tjarrojakka apatite-iron and Cu (-Au) occurrences, Kiruna area, northern Sweden. *Mineral Deposita* 40:409–434
- Frietsch R (1978) On the magmatic origin of iron ores of the Kiruna type. *Econ Geol* 73:478–485
- Frietsch R, Jan-Anders P (1995) Rare earth elements in apatite and magnetite in Kiruna-type iron ores and some other iron ore types. *Ore Geol Rev* 9:489–510
- Frietsch R, Tuisku P, Martinsson O, Perdahl JA (1997) Early Proterozoic Cu-(Au) and Fe ore deposits associated with regional Na-Cl metasomatism in northern Fennoscandia. *Ore Geol Rev* 12:1–34
- Geijer P (1910) Igneous rocks and iron ores of Kiirunavaara, Luossavaara and Tuollavaara. Scientific and practical researches in Lapland arranged by the Luossavaara-Kiirunavaara Aktiebolag - Geology of the Kiruna district, 2: Stockholm, p. 278
- Geijer P (1919) Recent developments at Kiruna. *SGU, C* 288:23
- Grigsby JD (1990) Detrital magnetite as a provenance indicator. *J Sediment Petrol* 60(6):940–951
- Groves DI, Bierlein FP, Meinert LD, Hitzman MW (2010) Iron oxide copper-gold (IOCG) through Earth's history: implications for origin, lithospheric setting, and distinction from other epigenic iron oxide deposits. *Econ Geol* 105:641–654
- Hallberg A, Bergman T, Gonzalez J, Larsson D, Morris GA, Perdahl JA, Ripa M, Niiranen T, Eilu P (2012) Metallogenic areas in Sweden. Survey of Finland, Special Paper 53:139–206
- Harlov DE, Andersson UB, Forster H-J, Nyström JO, Dulski P, Broman C (2002) Apatite-monzonite relations in the Kiirunavaara magnetite-apatite ore, northern Sweden. *Chem Geol* 191:47–72
- Henríquez F, Martín RF (1978) Crystal growth textures in magnetite flows and feeder dykes. El Laco, Chile. *Can Miner* 16:581–589
- Henríquez F, Naslund HR, Nyström JO, Vivallo W, Aguirre R, Dobbs FM, Lledó H (2003) New field evidence bearing on the origin of the El Laco magnetite deposit, northern Chile—a discussion. *Econ Geol* 98:1497–1502
- Hildebrand RS (1986) Kiruna-type deposits—their origin and relationship to intermediate subvolcanic plutons in the great bear magmatic zone, northwest Canada. *Econ Geol* 81:640–659
- Hitzman MW (2000) Iron oxide-Cu-Au deposits: what, where, when, and why. In T. M. Porter (Ed.), *Hydrothermal iron oxide copper-gold & related deposits a global perspective* (pp. 9–26). PGC Publishing, Adelaide
- Hitzman MW, Oreskes N, Einaudi MT (1992) Geological characteristics and tectonic setting of Proterozoic iron-oxide (Cu-U-Au-REE) deposits. *Precambrian Res* 58:241–287
- Jochum KP, Willbold M, Raczek I, Stoll B, Herwig K (2005) Chemical characterisation of the USGS reference glasses GSA-1G, GSC-1G, GSD-1G, GSE-1G, BCR-2G, BHVO-2G and BIR-1G using EPMA, ID-TIMS, ID-ICP-MS and LA-ICP-MS. *Geostandards and Geoanalytical Research* 29(3):285–302
- Kamenetsky VS, Charlier B, Zhitova L, Sharygin V, Davidson P, Feig S (2013) Magma chamber-scale liquid immiscibility in the Siberian Traps represented by melt pools in native iron. *Geology* 41(10):1091–1094
- Knipping JL, Bilenker LD, Simon AC, Reich M, Barra F, Deditius AP, Wälle M, Heinrich CA, Holtz F, Munizaga R (2015) Trace elements in magnetite from massive iron oxide-apatite deposits indicate a combined formation by igneous and magmatic-hydrothermal processes. *Geochim Cosmochim Acta* 171:15–38
- Lindsley DH (1976) The crystal chemistry and structure of oxide minerals as exemplified by the Fe-Ti oxides. In oxide minerals. Mineralogical Society of America, Short Course Notes 3:L-1 to L-60
- Lindsley DH (1991) Oxide minerals: petrologic and magnetic significance. *Reviews in Mineralogy, Volume 25*, Stony Brook, New York, USA
- LKAB (2015) Annual and sustainability report <http://www.lkab.com/en/>. Accessed 30 April 2016
- Loberg BEH, Horndahl A-K (1983) Ferride geochemistry of Swedish Precambrian iron ores. *Mineral Deposita* 18:487–504
- Martinsson O (1994) Greenstone and porphyry hosted ore deposits in northern Norrbotten. NUTEK report nr 92-00752P: Luleå, p. 31.
- Martinsson O (2004) Geology and metallogeny of the northern Norrbotten Fe-Cu-Au province: Society of Economic Geologists. *Guidebook Series* 33:131–148
- Martinsson O, Billström K, Broman C, Weihed P, Wanhainen C (2016) Metallogeny of the northern Norrbotten ore province, northern Fennoscandian shield with emphasis on IOCG and apatite-iron ore deposits. *Ore Geol Rev*. doi:10.1016/j.oregeorev.2016.02.011
- McCulloch MT, Gamble JA (1991) Geochemical and geodynamical constraints on subduction zone magmatism. *Earth Planet Sci Lett* 102:358–374
- Mehdilo A, Irannajad M (2010) Applied mineralogical studies on Iranian hard rock titanium deposit. *Journal of Minerals & Material Characterization & Engineering* 9(3):247–262
- Mucke A, Younessi R (1994) Magnetite-apatite deposits (Kiruna-type) along the Sanandaj-Sirjan zone and in the Bafq area. Iran. Associated with Ultramafic and Calcalkaline Rocks and Carbonatites: *Mineralogy and Petrology* 50:219–244
- Muller B, Axelsson MD, Bjorn O (2003) Trace elements in magnetite from Kiruna, northern Sweden, as determined by LA-ICP-MS. *GFF* 125:1–5
- Nadoll P, Angerer T, Mauk JL, French D, Walshe J (2014) The chemistry of hydrothermal magnetite: a review. *Ore Geol Rev* 61:1–32
- Nadoll P, Mauk JL, Leveille RA, Koenig AE (2015) Geochemistry of magnetite from porphyry Cu and skarn deposits in the southwestern United States. *Miner Deposita* 50:493–515
- Naranjo JA, Henríquez F, Nyström JO (2010) Subvolcanic contact metasomatism at El Laco Volcanic Complex, central Andes. *Andean Geol* 37:110–120
- Naslund HR, Henríquez FJ, Nyström JO, Vivallo W, Dobbs F (2002) Magmatic iron ores and associated mineralization: examples from the Chilean high Andes and Coastal Cordillera; in Porter, T.M. (Ed.). *Hydrothermal Iron Oxide Copper-Gold & Related Deposits: A Global Perspective*, PGC Publishing, Adelaide 2:207–226
- Nyström JO, Henríquez F (1994) Magmatic features of iron ores of the Kiruna type in Chile and Sweden; ore textures and magnetite geochemistry. *Econ Geol* 89:820–839
- Nyström JO, Billström K, Henríquez F, Fallick AE, Naslund HR (2008) Oxygen isotope composition of magnetite in iron ores of the Kiruna type in Chile and Sweden. *GFF* 130:177–188
- Nyström JO, Henríquez F, Naranjo JA, Naslund HR (2016) Magnetite spherules in pyroclastic iron ore at El Laco, Chile. *Am Mineral* 101:587–595
- Parák T (1975) Kiruna iron ores are not “intrusive-magmatic ores of the Kiruna type”. *Econ Geol* 70:1242–1258
- Park CF (1961) A magnetite “flow” in northern Chile. *Econ Geol* 56:431–436
- Paton C, Hellstrom J, Paul B, Woodhead J, Hergt J (2011) Iolite: freeware for the visualisation and processing of mass spectrometric data. *J Anal At Spectrom* 26:2508–2518. doi:10.1039/c1ja10172b
- Philpotts AR (1967) Origin of certain iron-titanium oxide and apatite rocks. *Econ Geol* 62:303–315
- Ramanaidou E, Wells M, Belton D (2008) Mineralogical and microchemical methods for the characterization of high-grade banded iron formation-derived iron ore. *SEG Reviews* 15:129–156
- Rhodes AL, Oreskes N (1999) Oxygen isotope composition of magnetite deposits at El Laco, Chile: evidence of formation from isotopically heavy fluids. *Soc of Econ Geol, Spec Pub* 7:333–351

- Romer RL, Martinsson O, Perdahl JA (1994) Geochronology of the Kiruna iron ores and hydrothermal alterations. *Econ Geol* 89: 1249–1261
- Rudnick R, Gao S (2003) Composition of the continental crust. *Treatise Geochem* 3:1–64
- Sabet-Mobarhan-Talab A, Alinia F, Ghannadpour S-S, Hezarkhani A (2015) Geology, geochemistry, and some genetic discussion of the Chadormalu iron oxide-apatite deposit, Bafq District, central Iran. *Arab J Geosci* 8:8399–8418
- Sillitoe RH (2003) Iron oxide-copper-gold deposits: an Andean view. *Mineral Deposita* 38:787–812. doi:10.1007/s00126-003-0379-7
- Sillitoe RH, Burrows DR (2002) New field evidence bearing on the origin of the El Laco magnetite deposit, northern Chile. *Econ Geol* 97: 1101–1109
- Storey CD, Smith MP, Jeffries TE (2007) In situ LA-ICP-MS U-Pb dating of metavolcanics of Norrbotten, Sweden: records of extended geological histories in complex titanite grains. *Chem Geol* 240:163–181
- Tassi F et al (2009) The magmatic- and hydrothermal-dominated fumarolic system at the active crater of Láscar volcano, northern Chile. *Bull Volcanol* 71:171–183
- Tornos F, Velasco F, Hanchar JM (2016) Iron oxide melts, magmatic magnetite and superheated magmatic-hydrothermal systems: the El Laco deposit, Chile. *Geology* 44(6):427–430
- Valley PM, Hanchar JM, Whitehouse MJ (2011) New insights on the evolution of the Lyon mountain granite and associated Kiruna-type magnetite-apatite deposits, Adirondack Mountains, New York state. *Geosphere* 7:357–389
- Velasco F, Tornos F (2012) Insights on the effects of the hydrothermal alteration in the El Laco magnetite deposit (Chile). *Revista de la Sociedad Española de Mineralogía* 16:210–211
- Velasco F, Tornos F, and Hanchar, JM (2016) Immiscible iron- and silica-rich melts and magnetite geochemistry at El Laco volcano (northern Chile): Evidence for a magmatic origin for the magnetite deposits. *Ore Geol Rev* 79:346–366
- Westhues A, Hanchar JM, Whitehouse MJ, Martinsson O (2016) New constraints on the timing of host rock emplacement, hydrothermal alteration and iron oxide apatite mineralization in and around Kiruna, Norrbotten region, northern Sweden. *Econ Geol*, in press
- Williams PJ, Hedenquist JW, Barton MD, Johnson DA, Fontbote L, de Haller A, Mark G, Oliver NHS, Marschik R, Thompson JFH, Goldfarb RJ, Richards JP (2005) Iron oxide copper-gold deposits; geology, space-time distribution, and possible modes of origin. *Econ Geol* 100:371–405
- Zipkin AM, Hanchar JM, Brooks AS, Grabowski MW, Thompson JC, Gomani-Chindebvu E (2015) Ochre fingerprints: Distinguishing among Malawian mineral pigment sources with Homogenized Ochre Chip LAICPMS. *Archaeometry* 57:297–317. doi:10.1111/arcm.12090